Title: Cortical microtubules act as a template to organize nano-scale patterning of the SEC/MUNC protein KEULE and exocytosis

Authors: Jelmer J. Lindeboom[1,2]*, Ryan Gutierrez[1,3], Viktor Kirik[4] and David W. Ehrhardt[1,3]*

Affiliations:

[1]Department of Plant Biology, Carnegie Institution for Science; Stanford, CA 94305, USA.

[2]Current Address: Novo Nordisk Foundation Center for Genomic Mechanism of Disease, Broad Institute of MIT and Harvard, MA 02142, USA.

[3]Department of Biology, Stanford University; Stanford, CA 94305, USA.

[4]School of Biological Sciences, Illinois State University; Normal, IL 61790, USA.

*Corresponding authors

Email: dehrhardt@carnegiescience.edu

jelmer@broadinstitute.org

Abstract

The microtubule cytoskeleton plays an important role in targeting and organizing exocytosis, enabling cellular morphogenesis, motility and polarized transport. However, in many cell types, the mechanisms by it does so are not well understood. Here, we identify the exocytotic protein KEULE, an essential SEC/MUNC, as a dynamic marker for exocytosis that forms clusters that are associated with and required for discrete exocytotic events in growing *Arabidopsis* cells. Live cell imaging and super-resolution image analysis revealed that KEULE clusters and exocytotic events are significantly enriched in ~180 nm wide linear domains that flank membrane-associated cortical microtubules, while being under-represented in adjacent domains ~520 nm wide. Thus, the cortical microtubule array acts as a highly organized and dynamic two-dimensional template that effectively redistributes and patterns exocytotic proteins and a significant portion of exocytotic traffic; a mechanism distinct from those previously described in which exocytotic targeting is achieved by vectorial motor-driven transport to destinations defined by microtubule plus ends. Microtubule arrays near or at the plasma membrane may play similar roles in organizing exocytosis in other cell types and organisms.

Main Text

Introduction

The ability to organize biomolecules at the cell cortex was a fundamental innovation in the evolution of cellular life, enabling essential biological functions including cellular morphogenesis, motility and polarized transport. Targeted exocytosis, non-random positioning and fusion of exocytotic vesicles at the plasma membrane, is a crucial mechanism for creating such cortical organization. Across phyla, the actin and microtubule cytoskeletons have been implicated in spatial organization of exocytosis. This functionality is exemplified in plant and fungal cells by cellular tip growth, and in animal cells by polarization of mammalian epithelia, cell migration and the positioning of focal adhesions[1,2]. The molecular polarity of microtubules plays an important role in how their function in exocytotic targeting is understood. For example, polarized arrays of microtubules created by nucleation from centralized organizing bodies - such as centrosomes or Golgi - can serve as directional tracks for motor-driven transport of exocytotic vesicles from where they are created in the cell interior to peripheral destinations at the plasma membrane[2,3]. More refined positioning of exocytosis is proposed to be accomplished by association of microtubule plus ends with specific locations at the plasma membrane, such as at or near focal adhesions [1]. Centrally polarized arrays of microtubules can also organize exocytosis through directed transport of factors that establish membrane domains that serve to target exocytotic traffic, such as that which drives tip growth in fission yeast[4]. However, many cells across diverse organisms feature interphase microtubule arrays that are not centrally organized and have architectures where microtubules are not clearly polarized with respect to the plasma membrane[5]. Acentrosomal arrays are required in important biological processes that require exocytosis, such as morphogenesis, but relatively little is understood about how they may function to target and pattern exocytotic traffic.

Gaining an understanding of exocytotic targeting mechanisms requires an ability to observe individual exocytotic events with respect to targeting machineries and a means to verify successful delivery of exocytotic cargo. Observing individual exocytosis events has been challenging in many cell models because microtubules, exocytotic vesicles and the machineries of exocytosis are often densely concentrated. Axially growing cells in the epidermis of higher plants have features that provide an excellent experimental platform to make such observations and for investigating how acentrosomal microtubule arrays may target and pattern exocytosis. In contrast to cells with microtubule arrays that are polarized with respect to the cell interior and the plasma membrane, these cells feature highly ordered arrays of microtubules that lie at the cell cortex in parallel to and in contact with the plasma membrane along their lattices. Large regions of the plasma membrane lie in a single focal plane, where the individual microtubules and microtubule bundles that constitute these arrays are easily visualized due to their quasi-2-dimensional nature and comparatively low density[6]. In previous studies, we found that cellulose synthase complexes (CSCs), large integral membrane protein complexes that synthesize and extrude cellulose into the cell wall, can be used to observe individual exocytotic events at the plasma membrane by allowing dynamic tracking of both exocytotic vesicles and the successful delivery of cargo to the plasma membrane[7–9]. By tracking CSCs while simultaneously imaging dynamic cortical arrays, we discovered that CSCs were preferentially delivered to the plasma membrane at locations defined by microtubules. This targeting did not involve vesicular transport along microtubules, nor did it involve defining exocytotic domains by end-on association of microtubule ends with the plasma membrane[10], thus suggesting a previously

undescribed mechanism for microtubule-dependent exocytotic targeting. However, CSC's themselves have been shown to interact with microtubules via a specific protein (CSI1), a mechanism that can also tether CSC-containing vesicles and organelles to microtubules[11–14]. Thus, it was not clear if this exocytotic targeting mechanism may be widely employed or if it is unique to delivery of CSCs to the plasma membrane.

Microtubule targeting of exocytosis is of special interest in the context of plant cell growth because ordered cortical microtubule arrays are essential to create functional cell shape. Depolymerization of microtubules by the drug oryzalin causes isotropic growth and a complete loss of genetically determined cell shape. The predominant hypothesis for the function of cortical microtubules in directing cell growth is that they guide the trajectories of CSCs as they synthesize and extrude cellulose microfibrils into the cell wall, thus creating material and mechanical anisotropy to direct expansion of the cell wall under tension by high in turgor. The hypothesis that cortical microtubules guide the trajectories of CSCs was microtubules was confirmed by live cell imaging studies[15]. However, disruption of both microtubule guidance of CSCs and delivery of CSCs to the plasma membrane in *csi1* null mutants causes only a modest loss of cell growth anisotropy[11,12,14]. In addition, although complete loss of growth anisotropy is caused by microtubule depolymerization, this phenotype is not due to a loss of CSC delivery[10] nor a lack of ordering in CSC trajectories[16–18], and oryzalin treated cells continue to grow at near normal rates[19]. These observations suggest that cortical microtubules arrays have additional important functions in directing cell shape, prompting us to ask if cortical microtubules may guide cellular morphogenesis by acting as a general targeting mechanism, beyond CSC's, to pattern exocytosis during cell growth.

To determine if exocytosis in growing plant cells is broadly patterned by cortical microtubule targeting, we require a dynamic biological marker that identifies single exocytotic events and is involved in a wide range of exocytotic traffic to the plasma membrane. To date, such a marker has not been identified. Imaging studies of core exocytotic proteins, including soluble *N*-ethylmaleimide-sensitive factor attachment protein receptors (SNARE proteins)[20–22] and components of the exocyst complex[23,24], have not revealed a clear relationship between the presence and dynamics of these proteins with verified exocytosis events nor have they shown association of these proteins with microtubules[24].

SM proteins are essential regulators of SNARE-mediated vesicle fusion. In exocytosis, SNARE proteins anchored to the vesicle interact with those on the plasma membrane and form a membrane bridging complex with other partners that enables membrane fusion[25–27]. The soluble SM proteins are known to bind to SNAREs, and evidence from genetic studies together with *in vivo* and *in vitro* experiments suggest they function in vesicle docking, SNARE complex assembly and vesicle fusion [28–33]. In plants, the *Arabidopsis* Sec1 homolog KEULE was identified in a genetic screen for embryonic pattern mutants[34], where loss of function mutations are lethal, causing bloated and multinucleate cells[35]. Consistent with other SM proteins, KEULE interacts genetically and biochemically with Qa-SNAREs, specifically KNOLLE (SYP111) and SYP121, and has been shown to play essential roles in cell plate assembly during cytokinesis and exocytotic traffic to the plasma membrane[20,36–40]. The demonstrated function of KEULE in exocytosis, combined with its severe loss of function phenotype due to lack of exocytosis suggested that KEULE might serve as an excellent candidate for a generalized reporter of exocytosis.

The molecular and structural mechanisms by which SM proteins interact with and regulate SNARE complex assembly have investigated intensively by genetic, biochemical, *in vitro* and structural studies[28–33], and SM proteins have been imaged in live cells in several systems[41–48]. However, important features of their behaviors and biological function in living cells remain to be uncovered. These questions include the fine scale cellular distributions of SM proteins and clusters, the association of SM clusters with exocytosis events, the relationship of these exocytosis events to potential organizing machineries and the dynamics of SM assembly and loss at exocytosis sites, especially prior to and during vesicle fusion.

Here, we develop and apply automated and high precision analysis methods to detect and track tens of thousands of individual fluorescently-tagged KEULE clusters to investigate their dynamics and to map their positions at the plasma membrane in living cells. We evaluate these clusters as exocytotic events by use of CSCs as a validated cargo and employ genetic analysis to test for the function of KEULE in CSC delivery. Finally, we employ high precision mapping of KEULE clusters and microtubules, combined with Bayesian methods, to quantitatively investigate the cortical microtubule cytoskeleton as a template in patterning exocytosis.

Results

Functional dynamics of tdTomato-KEULE cluster formation

To visualize KEULE protein *in vivo*, we created a tdTomato-KEULE fluorescent reporter constructed from the chromosomal gene with native upstream regulatory sequence and introduced it into *Arabidopsis* plants heterozygous for a *keule* loss of function allele. To obtain plants for study of KEULE localization and dynamics, we screened for self-fertilized progeny of these transgenic plants that exhibited rescue of *keule* mutant phenotype by the tagged KEULE protein. These plants exhibited full rescue of plant growth and development through the 5-day seedling stage used for our further studies (Fig. S1, Methods).

In dark-grown *Arabidopsis* hypocotyl cells expressing the tdTomato-KEULE construct, we observed KEULE signal appear as densely distributed and temporally dynamic puncta at the plasma membrane (Fig. 1A). The dynamics of signal increase and decay were apparent in time-lapse movies (Movie S1), kymographs of signal intensity over time along transect lines (Fig. 1B) and in sequential image samples of individual puncta (Fig. 1C). In all, a steady increase in signal intensity was observed, followed by an abrupt decrease and disappearance of signal. This behavior indicates the accumulation and loss of many fluorescently labeled KEULE proteins, which we will refer to hereafter as clusters.

The dynamics of tdTomato-KEULE accumulation and disappearance are presumably related to its function. Therefore, we reasoned that a quantitative and robust picture of KEULE cluster dynamics would be useful in gaining insight into the underlying molecular mechanisms of exocytosis. To accomplish this, we collected a large-scale and high-resolution dataset comprising thousands of individual events. We acquired streamed images at 200 ms intervals and performed automated detection and frame-to-frame linking of KEULE cluster signal using µTrack[49]. This track information was then used to extract position and intensity information by Maximum Likelihood Estimate 2D Gaussian fitting[50] (for details see Methods, Movie S2). To define events of signal appearance, accumulation and loss, we used a minimum sample of 4 sequential acquisitions, which made our shortest measured lifetimes approximately 800 ms. The

lifetime distribution of tdTomato-KEULE clusters showed a large range, from this minimal event length of 800 ms to over half a minute. The data followed a roughly exponential distribution with a mean of 2.34 s and ~95% of lifetimes being less than 7 seconds long (Fig. 1D).

The large lifetime range of observed KEULE cluster events might represent a collection of functional classes. If so, such classes may by differentiated by their kinetics. To assess the kinetics KEULE signal accumulation and loss, and to ask if these kinetics might vary as a function of cluster lifetime, we leveraged our large data set to calculate KEULE kinetics for each 200 ms lifetime increment. Fig. 1E shows average intensities for all observed clusters with lifetimes of 4.2, 4.4 and 4.6 s. All these plots show a similar pattern: an initial steep rise in intensity, followed by a steady increase, then a short plateau phase, and ending with a sharp decrease. When we extended this analysis over a larger range of lifetimes, we observed evidence that the shorter-lived events accumulated tdTomato-KEULE intensity at a slower rate, suggesting they might be a functionally different class (Fig. 1F). At longer lifetimes, the plateau phase became more extended, suggesting that these events may be paused or stalled (Fig. 1F). To examine further these differences in accumulation kinetics as a function of cluster lifetime, we grouped events into three classes; short (0.8 to 1.6s), medium (1.8 to 6.2s) and long (6.4+s) – and then averaged the intensities at each 200 msec timepoint (Fig. 1G, for details see Methods). The timepoints following the plateau phase were omitted to reveal better differences or similarities in signal accumulation. This analysis confirmed that, indeed, the short events show significantly slower signal accumulation (Fig. 1G). Interestingly, the medium and long tdTomato-KEULE cluster lifetimes show nearly identical trends in signal intensity accumulation over time, indicating that they might be part of the same functional population during KEULE recruitment/assembly. It is noteworthy that for events up to ~5s, longer-lasting events reach a higher maximum cluster signal intensity. A possible explanation for this phenomenon is that larger vesicles require a larger area for membrane fusion and therefore more KEULE. Unlike the medium class, the long class exhibited a prolonged plateau phase, possibly indicating stalled exocytosis events or alternatively, an extended checkpoint for a class of exocytosis events involving a large amount of KEULE, and therefore perhaps larger exocytotic vesicles.

Clusters of tdTomato-KEULE coincide with CSC delivery to the plasma membrane

To place SM protein accumulation in context of functional exocytosis, we took advantage of our previous work on delivery of CSCs to the plasma membrane[7]. CSCs are assembled in the Golgi system from multiple CESA catalytic subunits[51,52], move through the trans-Golgi network (TGN) and are budded off into vesicles that fuse with the plasma membrane[7]. Because CSCs are formed of multiple CESA subunits, they can be labeled by fluorescent proteins in sufficient number to allow their detection and the tracking of individual complexes during the process of exocytosis. Labeled vesicles display rapid and erratic dynamics that abruptly become stabilized at the optical plane of the plasma membrane with a mean duration of about 60 seconds, followed by a transition to slow, steady and typically linear motility of between 250 and 450 nm/min. The transition erratic to static movement is interpreted as evidence for vesicular capture and tethering at the plasma membrane, and the transition to slow and steady movement indicates successful vesicle fusion and delivery of CSCs, which are propelled by the synthesis and extrusion of cellulose microfibrils[15,17]. This stereotyped behavior makes CSCs an excellent reporter for successful exocytosis, revealing a time and place for vesicle tethering, and distinguishing vesicle tethering at the plasma membrane from successful vesicle fusion and cargo delivery.

To visualize KEULE together with CSCs, we generated plants that express tdTomato-KEULE and CIT-CESA6, a catalytic CSC subunit labeled with Citrine fluorescent protein[53] in a *keule*/*cesa6* double mutant background (Methods). CIT-CESA6 signal is relatively dense in the plasma membrane of rapidly growing cells so we photobleached the CIT-CESA6 signal over a region of the plasma membrane to aid detection of new CSC arrivals and their relation to td-Tomato-KEULE signal (Fig. 2A, Movie S3). For each CSC arrival at the optical plane of the plasma membrane, we determined the first frame in which the CESA6 signal became stationary (an indication of interaction and tethering at the plasma membrane). We then identified the nearest KEULE cluster in a range of -10 to 50 seconds of the first stable CESA6 frame and determined the distance between the centroid of the CESA6 signal and the centroid of the nearest KEULE signal by maximum likelihood 2D Gaussian fitting (See Methods). A search range starting at -10 seconds was chosen because the exact frame of stationary transitions was in some cases obscured by signal from clusters of other labeled organelles such as Golgi bodies and TGN. If KEULE is involved in the exocytotic delivery of CSCs to the plasma membrane, we expect to observe co-localization between CSC delivery events and KEULE clusters. However, CSC deliveries, as defined by static tracks, are relatively sparse and long lived as compared to KEULE cluster events, so some degree of colocalization in space and time is expected by chance alone. To assess statistically the spatial and temporal association of CSC delivery events and KEULE clusters, we generated a simulated dataset of random locations within the photobleaching areas and identified the nearest KEULE spot to the random spots within the same time window we used for our experimental observations. We then compared the distributions of distances to the nearest KEULE cluster between the observed CSC deliveries and the simulated spots (Fig. 2B and D) and found that the experimental data were strongly skewed to shorter distances ($p < 1E-06$, Kolmogorov-Smirnov test). The pattern of over- and under-representation of observed with respect to simulated data is more easily seen in a plot of the bin-by bin differences where shorter KEULE-microtubule distances are seen to be over-represented in bins below 200 nm and underrepresented in bins of longer values (Fig. 2C). Using a Bayesian method (See Methods), we found that the most likely values of the experimental biases from the null hypothesis of a random association were significantly above that expected by chance alone for distance bins below 120 nm (Fig 2E and F) and significantly lower than expected in bins of longer distances from 200 to 480 nm. Based on these data we defined colocalization as observing a KEULE cluster centroid within 200 nm from the position of CSC signal in the first frame in which it was observed to stabilize (and in a time window of -10 to 50 seconds around that frame). By these criteria, we found colocalization in 81% (157 out of 194) of observed delivery events compared to 29% (13035 out of 45051) of random locations at the plasma membrane ($p < 1.4E-50$, Fisher's exact test).

We considered that our automated experimental protocol may allow for underestimation of colocalization between CSC delivery and KEULE. For example, the time interval used for these experiments is 2.11 s, of which 400 ms is used for tdTomato-KEULE excitation and image acquisition. Since a substantial portion of KEULE cluster lifetimes is shorter than the ~1.7 s gaps between image acquisitions, we do not expect to detect all KEULE clusters within the -10 to 50 second experimental window. In addition, not all excited KEULE foci are successfully identified by the spot detection and filtering routines used for large-scale data collection. To understand how these two cases, no excitation and no detection, affect our colocalization results, we performed a hand-curated analysis using a custom MATLAB GUI. For each CSC delivery, we examined whether there was overlap of KEULE signal with the centroid of the CSC signal in the

first frame of positionally stable KEULE signal (tethering frame). We found that in 92% (159 out of 172) of the cases, KEULE signal was observed to overlap the CSC position in the tethering frame within -10 to 50 s of CSC stabilization, suggesting that our automated analysis, while free of possible observer bias, may underestimate the true degree of colocalization frequency of CSC exocytosis events and KEULE.

If KEULE clusters function in CSC exocytosis after vesicle tethering, we expect that not only should they colocalize with CSC signal, but that the time intervals between vesicle tethering and the recruitment of KEULE should have a non-random distribution. We tested this prediction by comparing the delay times for arrival of the nearest KEULE spot following the tethering frame in the observed vs the simulated KEULE data sets. The observed delay time distribution was significantly different from the random distribution of the simulated data ($p < 7.8E-04$ Mann-Whitney U test) (Fig. 3B), having a peaked distribution with a median of 2.111 s and a mean of 7.92 s, suggesting that KEULE is recruited and functions within a several seconds after the CSC vesicle is stabilized and tethered at the plasma membrane. These data now provide insight into the kinetics of SM protein recruitment to the site of exocytosis and the time of vesicle fusion following exocytotic vesicle stabilization and tethering at the plant cell plasma membrane.

The durations of KEULE clusters associated with CES deliveries had a distribution similar in character to that observed For KEULE clusters in general (Fig. 3B, compare to Fig.1D), with both appearing roughly exponential but long tailed. While lifetimes of clusters associated with CESA deliveries spanned a similar range of durations, those associated with CESA delivery were observed to have a significant bias towards longer values, with clusters associated with CESA having a median duration of 4.3 seconds, as compared to 2.3 seconds for clusters in general. To test the significant of this observed bias, we compared the relative frequencies of durations longer than two seconds and found a highly significant difference - 59% vs 37% for CESA delivery-associated KEULE clusters events vs clusters in general (Fig. 3C, $p=6.07E-09$ Fisher's exact test). These results indicate that both short-lived and long-lived KEULE clusters are associated with verified exocytosis events and that those associated with CESA complexes are modestly biased towards longer lifetimes.

Our data show that KEULE clusters are associated with confirmed sites of CSC exocytosis in both space and time, but is KEULE function required for CSC exocytosis? To answer this question, we quantified CSC delivery in selfed progeny of parental plants homozygous for a transgene expressing CIT-CESA6, heterozygous for a *tdTomato-KEULE* allele, and homozygous for *cesa6* and *keule* loss of function alleles (See Methods). Seedlings tested for loss of KEULE function were identified by morphological *keule* phenotype (severely reduced in size, large and misshaped cells) and little to no tdTomato-KEULE signal. In these mutant seedlings, we found that the CSC delivery rate was reduced by over 17-fold as compared to that in wildtype ($p<0.0001$, Wilcoxon two sample test, Fig. 2G). Taken together our results indicate that KEULE plays an essential role in plasma membrane delivery of primary CSCs, and that CSC delivery is spatially and temporally associated with KEULE clusters which display stereotyped dynamics of formation and loss.

KEULE dynamics are sensitive to drugs and treatments that reduce exocytosis

We previously reported that the number of active CSCs in the plasma membrane were rapidly and significantly reduced by treatment with mannitol (osmotic stress) and the herbicide

299 isoxaben[7]. Measurements of CSC delivery revealed that mannitol treatment also caused a 100-
300 fold reduction in the delivery rate of CSC's, indicating that CSC loss at the plasma membrane
301 was likely caused primarily by inhibition of exocytosis. At what step or steps of the secretory
302 pathway this inhibition of exocytosis by osmotic stress is imposed is not known. Isoxaben has
303 been characterized as a specific cellulose synthase complex inhibitor[54], but its mode of action is
304 not well understood. Here we (1) determine if isoxaben treatment also reduces CSC exocytosis
305 and (2) ask if analysis of KEULE dynamics may provide insight into how osmotic stress and
306 isoxaben act to inhibit exocytosis.

307 To address the above questions, we treated seedlings expressing tdTomato-KEULE and
308 Cit-CESA6 with either 200 mM mannitol, 100nM isoxaben or carrier only (0.01% DMSO,
309 mock) and assayed CSC delivery to the plasma membrane as described above. We found that,
310 like osmotic stress caused by mannitol, isoxaben is also a potent inhibitor of CSC exocytosis,
311 reducing CSC delivery rate by ~70 fold (Fig. S2). The overall frequencies of KEULE cluster
312 formation after both mannitol and isoxaben treatment were not significantly lower than that
313 observed for mock treatment, indicating that neither acts to absolutely block KEULE recruitment
314 and that any differences in initial cluster formation are not detected over the cluster population as
315 a whole (Fig. S3A). However, when comparing accumulation dynamics we observed striking
316 differences among treatments (Fig. S3B, C). In cells treated with mannitol, both short and
317 intermediate duration events (0.8-1.6s and 1.8-6.2s, respectively) accumulated tdTomato-
318 KEULE signal more slowly and to lower final levels on average than observed in mock treated
319 cells (Fig. S3B). Intriguingly, the dynamics of long duration clusters (6.4 s or longer) exhibited a
320 markedly different pattern. In both mock and isoxaben treated cells, KEULE signal trajectories
321 tracked each other closely for the first 5 s or so, after which signal plateaued in mock treated
322 cells. However, in mannitol treated cells signal did not plateau, but continued to increase steadily
323 until the transition to rapid signal loss (Fig. S3B). These data suggest that there may be two
324 different mechanisms by which mannitol treatment and osmotic stress affects KEULE dynamics,
325 depending on their duration class: one mechanism that acts negatively and from cluster inception
326 that reduces the rate of KEULE accumulation, and one which acts at a later stage that prevents
327 transition to the normally occurring plateau stage. By contrast, we observed that isoxaben
328 treatment slowed accumulation of tdTomato-KEULE across events of all durations (Fig. S3C).

329 We observed related differences among treatments in KEULE cluster lifetimes. In
330 comparing the distributions of cluster lifetimes in mock and mannitol treated cells, a bimodal
331 effect was again observed, with both shorter and longer lifetimes being over-represented in
332 comparison with mock treatment (and intermediate events being under-represented) (Fig S4A, B,
333 D). As was the case with intensity dynamics, isoxoben treatment showed more of a unimodal
334 effect, with the lifetime distribution being shifted to the left (Fig. S4B, C, E). Mannitol and
335 isoxaben also caused diverging effects on persistence of KEULE clusters, as assessed by survival
336 analysis (Fig. S4F, G). Taken together, our data show that KEULE cluster dynamics are sensitive
337 to perturbations that affect exocytosis and reveal evidence that mannitol and isoxoben treatments
338 affect these dynamics in distinct ways, suggesting they may perturb exocytosis by different
339 mechanisms.

340

341 **Cortical microtubules pattern KEULE cluster distribution and exocytosis**

342 Having established dynamic KUELE clusters as markers of exocytotic events, we noted
343 that the flux of KEULE cluster formation, 144 events per μm^2 per h (Fig. S3A), is ~85-fold
344 higher than that of CSC delivery (1.59 evens per µm2 per h, Fig. 2G). We therefore utilized
345 dynamic imaging of KEULE and microtubules together to ask if cortical microtubules pattern the
346 distribution of KEULE protein and to determine if targeting of exocytosis is specific for CSCs or
347 if it is a broad and fundamental function for the cortical microtubule cytoskeleton in growing
348 plant cells. Further, we took advantage of the ability to detect thousands of KEULE clusters to
349 map the spatial range of influence of microtubule targeting with super-resolved precision.

350 To visualize KEULE cluster events together with cortical microtubules, we performed
351 live cell imaging at 1 second intervals in hypocotyl cells of *Arabidopsis* seedlings expressing
352 GFP-TUA5 and tdTomato-KEULE in a *keule* knock-out background (Fig. 4A, Movie S4). We
353 tracked individual KEULE events at the plasma membrane and used MLEwG fitting to extract
354 precise positional information (Fig. 4B, Methods), after which we identified the frame with peak
355 signal intensity as the reference point for each detected KEULE cluster position (Fig. 4C panels
356 1-3). We then measured signal intensity in the microtubule channel along a series of scan lines
357 that were rotated at 9° intervals around the centroid of the KEULE cluster (Methods and Fig. 4C
358 panel 4). On each of these scan lines, we detected all microtubule signal peaks and fit them with
359 a modified quasi-1-dimensional MLEwG fit (Methods, Fig. 4D). Since the microtubule signal is
360 best represented as a quasi-1-dimenional Gaussian orthogonal to the microtubule axis, we
361 determined the orientation of the nearest microtubule as identified by peak analysis and used the
362 scan line most orthogonal to the microtubule angle for determining the location of the
363 microtubule central axis closest to the KEULE spot in question (Fig. 4C, panel 5). For example,
364 the intensity of KEULE signal in photoelectrons for the most orthogonal scan line in Fig. 4C
365 panel 5 is shown in Fig. 4D panel 1, the triple Gaussian MLEw1dG fit in panel 2, and the
366 decomposed individual peak fits in panel 3. We used the fit positional coordinates of the nearest
367 microtubule signal peak and the KEULE cluster to calculate the distance and the photoelectron
368 fit values to estimate the standard error of the measurement (See Methods and Fig. 4C panel 6).
369 We repeated this process for all detected KEULE tracks in each movie to assess the spatial
370 relationship between KEULE clusters and the nearest microtubules to those clusters (Fig. 4E,
371 panel 1).

372 To ask if the measured distribution of KEULE to microtubule distances differs from that
373 expected if KEULE cluster positions are independent of microtubule locations (the null
374 hypothesis), we first needed to determine what the expected distributions are under the null
375 hypothesis when our detection and analysis routines are applied to the image datasets we used
376 for our experimental observations. For example, microtubule array structure, which varies within
377 and among cells, will have a strong influence on this distribution, as will the dimensions of our
378 detection kernels. Therefore, we generated a simulated set of random locations within each
379 region of interest across all image frames in the movies and calculated the distances from these
380 synthetic KEULE foci to the nearest microtubule (Fig. 4E, panel 2). When the experimental and
381 expected distributions were plotted together as relative frequencies, they showed evidence for
382 distinct differences (Fig. 5A). The spatial pattern of under- and over-representation is more
383 easily visualized in a plot of the differences between observed and expected frequencies (Fig.
384 5B). To quantify over- or under-representation of the experimental data given the expected data
385 under the null hypotheses, we used a Bayesian method to determine the most likely positive or
386 negative bias at each distance bin (Fig. 5C and D and Methods). We found that at KEULE-
387 microtubule distances smaller than 180 nm, the maximum likelihood bias was significantly

388 positive (more frequent than expected) and between 180 and 700 nm this bias was significantly
389 negative (less frequent than expected). At distances > 700 nm we again found a positive, but
390 smaller, bias (Fig. 5D).

391 When examining patterns of KEULE foci, we also observed that sites of previous
392 exocytosis events were 3.4 times more likely to show consecutive exocytosis events within 60
393 seconds than random sites at the plasma membrane (Fig. S5A-E,G). Such "hot spots" were also
394 significantly over-represented within 180 nm of microtubules, but only modestly so (1.25 times
395 more likely) (Fig. S5F,G).

396 Taken together, our results reveal that microtubules spatially organize exocytosis
397 machinery by increasing the frequency of KEULE cluster formation within about 180 nm of the
398 center of the microtubules, a distance about 7 times the dimension of a single microtubule, while
399 at the same time decreasing the probability of KEULE cluster formation distally over a region
400 that is about 3 times as wide. This acts effectively as a concentrating mechanism for KEULE
401 cluster events that is patterned by cortical microtubule organization. As these KEULE clusters
402 overlap heavily in their dynamic characteristics with those observed associated with validated
403 exocytosis events of CSCs, this is strong evidence that microtubule organization of exocytosis is
404 not confined to guiding insertion of CSCs but is a more generalized feature of exocytosis in
405 growing plant cells.

406 **Discussion**

407 To assess imaging of SM/KEULE clusters as a general marker for exocytosis it was
408 important to answer two questions; if there are different types of signal foci that may represent
409 multiple types of cellular structures or functional events, and what features of signal dynamics
410 are associated with exocytotic events. For example, some exocytotic proteins, including V-
411 SNARES and constituents of the exocyst, have been shown to arrive at the site of exocytosis on
412 exocytotic vesicles themselves, while others reside in the cytosol or associate with the plasma
413 membrane and are recruited to the exocytosis site. While we found some evidence for KEULE
414 signal on cytosolic organelles, these foci were relatively rare and were easily identified by their
415 positional dynamics. Further, in experiments using labeled CSCs as a trackable exocytotic cargo,
416 no KEULE signal was detected arriving at validated exocytosis sites on CSC-containing vesicles,
417 indicating that KEULE clusters at the plasma membrane form by recruitment of KEULE to sites
418 of exocytosis after arrival and interaction of cargo-carrying organelles with the plasma
419 membrane. KEULE assembly dynamics of clusters associated with CSC delivery had similar
420 characteristics as the KEULE population in general, including a wide range of cluster lifetimes
421 from a couple of seconds to half a minute and stereotyped dynamics of signal accumulation and
422 loss. The demonstrated functions of SM proteins in mediating SNARE complex formation and
423 membrane fusion, together with their stereotyped dynamics and tight association with CSC
424 delivery, indicate that dynamic KEULE clusters are valuable markers of individual exocytotic
425 events.

426 Our measurements of thousands of KEULE clusters at the plasma allowed us to analyze
427 patterns of signal accumulation and loss as a function of varying cluster duration - revealing
428 features of, and raising new questions about, the underlying mechanisms of exocytotic
429 machinery assembly, maturation and resolution. Over all durations, KEULE recruitment features
430 an initial a phase of rapid accumulation, followed by continued recruitment at a slower rate. This
431 pattern suggests two phases of recruitment with different kinetics. The second rising phase is

near linear, indicating a near constant rate of addition over time, characteristic of mechanism such as polymerization, rather than recruitment of SM proteins to a fixed number of pre-existing binding sites. Such a kinetic might be consistent with the sequential addition of SM-bound SNARE-PINs to a growing chain of laterally-interacting SNARE-PINs at the vesicle-plasma membrane interface[55–57]. This accumulation phase ends and transitions to a plateau, after which signal abruptly decays to non-detectible levels. Both the final signal level and the length of the pause state correlate positively with cluster assembly time, with longer assembly times having higher signal levels and longer pause durations. Over the population of observed events, global peak signal is reached at durations of about 6 seconds, after which longer events involve no further signal accumulation but feature only lengthened plateau times. The plateau phase could represent a state where all the SNARE complexes required have been recruited to the fusion site and the components of the fusion super complex are transitioning to a functionally competent state prior to the enactment of membrane fusion. The plateau could also reflect an assembly checkpoint. Previous *in vitro* studies have found that greater numbers of SNARE proteins are recruited to interfaces of large vesicles and planar membranes[58,59]. It is possible, therefore, that our measurements of KEULE dynamics are shaped in part by a distribution of vesicle sizes, with longer assembly phases that build a brighter SM signal representing assembly of exocytotic machinery at larger vesicles.

We found that KEULE dynamics were changed when we disrupted exocytosis with osmotic stress by treatment with mannitol, or by application of a drug, isoxaben. The changes in dynamics were qualitatively different for the two antagonists, indicating that they likely act on different processes affecting exocytosis. These observations indicate that KEULE dynamics, which indicate functional aspects of vesicle fusion, are a sensitive and useful readout, or marker, for studying exocytosis and agents that disrupt or alter exocytosis.

High resolution mapping and Bayesian statistical analysis of individual exocytosis events marked by KEULE clusters revealed that these events are not randomly distributed in growing hypocotyl cells but are significantly over-represented in domains defined by the cortical microtubule array. This patterning of exocytosis differs from previously described mechanisms for exocytosis targeting by microtubules. In the latter, the positioning of microtubule plus ends define the locations for motor-transported delivery of either the exocytotic vesicles themselves or proteins that act in defining exocytotic domains. By contrast, our data indicate that every part of microtubule is associated with exocytosis targeting, making the entire cortical array a dynamic and steerable template for exocytotic patterning and organization of the cell cortex (Fig, 6A).

Our high precision measurements of both microtubule and KEULE cluster locations revealed that microtubules pattern exocytosis both positively and negatively and do so over spatial domains much larger than the scale of microtubules and microtubule bundles. Single microtubules and bundles of two polymers are ~25 nm and ~75 nm wide at the plant cell cortex, respectively[60], whereas the combined width of over-represented and under-represented domains was measured to be ~700 nm. The mean spacing between ordered microtubules and microtubules bundles in elongating hypocotyl cells is about twice this distance[61], indicating that microtubules influence exocytosis over most of the observed plasma membrane these cells (Fig. 6B). In addition, the combination of narrower elevated domains coupled with wider depleted domains of elevated exocytosis frequency suggests a concentrating effect that further enhances the relative difference in exocytosis adjacent to microtubules as compared to distances several hundred nanometers away.

One mechanism that could explain the spatial scales of these microtubule-associated domains is direct interaction of exocytotic vesicles with cortical microtubules, such as we previously observed for vesicles containing CSC's[7,62]. Microtubule-tethered vesicles might capture local KEULE associated with the plasma membrane, perhaps as bound to SNARE partners such as SYP121[36], depleting KEULE concentration in the nearby plasma membrane and making exocytosis there less likely, thus creating the observed zones of reduced exocytosis (Fig. 6B). Alternatively, upstream exocytotic machinery, such as plasma-membrane associated components of the exocyst complex, might be recruited by a microtubule-organized membrane domain, elevating location concentration while causing depletion and thus vesicle capture at a distance (Fig. 6B). Evidence that such microtubule-organized membrane domains might exist has been suggested by observations of the plasma membrane associated actin polymerase Formin1, which reveals narrow "dark" linear domains defined by cortical microtubules where fluorescently-tagged Formin1 is excluded[63].

The observed flux of KEULE clusters per unit area and time was about 90-fold higher than that measured for CSC delivery, therefore far more exocytosis events are associated with domains defined by microtubules than can be accounted for by CSC delivery alone, implying either that many or most exocytosis events in these cells are influenced by microtubules to some degree, or that a quantitatively significant subpopulation of specialized traffic is redistributed, ~13% of KEULE associated events as measured by our analysis. One possibility for specialized exocytotic traffic targeted by cortical microtubules are cargoes involved in cell wall biosynthesis and cell wall expansion. Supporting this idea is that KEULE has been shown to be an essential partner of the Qa-SNARE SYP121, which is implicated by a growing body of evidence in mediating exocytosis required for cell growth and expansion[21,36,37,64,65]. Cellulose is synthesized at the plasma membrane, while many other structural oligosaccharides, such as pectins[66], and wall-active proteins, such as expansins[67], are secreted. Targeting this exocytotic traffic by cortical microtubule arrays to the same locations where newly synthesized cellulose microfibrils are also being laid down could help coordinate the assembly of these diverse components to build a functional cell wall. In addition to coordination of wall assembly, it is possible that the patterned delivery of cell wall oligosaccharides and cell wall active proteins could itself act to support the anisotropic expansion of cell walls required to create specific cell shape. Targeting the delivery of proteins and other molecules that promote wall remodeling by ordered microtubule arrays could create linear and parallel microdomains of increased wall extendibility that lie perpendicular to the main axis of the cell growth - shaping the anisotropy of cell wall expansion in the same direction as proposed in prevailing models for constraint of expansion by cellulose microfibrils organized by microtubules[68]. As discussed in the introduction of this manuscript, an important reason to consider alternative functions for cortical microtubules arrays in guiding cell wall expansion and cell shape is that experimental evidence suggests that guidance of cellulose deposition and CSC delivery alone is not sufficient to explain the anisotropy of cell wall expansion and cell growth. Microtubule targeting of cell wall-active factors by exocytosis could also help explain redirection of cell growth in response to signals, such as blue-light stimulation of phototrophic growth. Perception of blue light by Phototropin receptors causes a rapid 90° reorientation of cortical microtubule arrays[69], but the following redirection of expansion cannot be easily explained by directed cellulose deposition model since previously synthesized cellulose is deposited perpendicular to the direction of expansion. Microtubule patterning of cell wall-active factors might allow for redirection of cell expansion regardless of cellulose orientation.

The insights we gained into patterning of exocytosis by cortical microtubule arrays were enabled by utilizing an experimental platform and methods that made detecting, measuring and assessing many thousands of discreet molecular events possible. A protein implicated in mediating a broad swath of a cell's exocytotic traffic might be expected to be subject to a range of targeting mechanisms, including no targeting at all. Such a background could easily obscure a meaningful association between the protein and an hypothesized targeting machinery. Very large sample sizes and appropriate methods to test for meaningful associations, such as we employed here, can robustly reveal such relationships.

The fact that growing plant cells have a planar microtubule array that is associated with the plasma membrane, and that exocytotic events as marked by KEULE protein are of relatively low density, has provided an excellent platform to study how microtubules pattern exocytosis, and do so at the level of individual exocytotic events. When we consider cellular microtubule function in cellular trafficking, we typically think of directed transport of cargos by kinesins and dynein. In contrast, this work highlights that microtubules can also function as scaffolds for organizing exocytosis. This scaffolding function for microtubules might be considered in other systems where there is indirect evidence that microtubules regulate exocytosis where they interact with the plasma membrane, such as in focal adhesions and neuronal growth cones[1,70,71]. In addition, scaffolded guidance of exocytosis should also be considered in the context of disease. For example, amyotrophic lateral sclerosis (ALS) risk is associated with genetic variants which reduce levels of functional UNC13A[72,73], and with genetic variation within several microtubule associated proteins[72–75]. It is possible that these proteins all converge on the same biological process of microtubule dependent patterning of exocytosis.

545 **Materials and Methods**

546 Generation of transgenic lines

547 The *pKEULE-tdTomato-KEULE* construct was generated by modifying the Gateway-
548 compatible vector pMDC43[76]. A 2049-bp region immediately upstream of the start codon of
549 *KEULE* (At1g12360) was amplified with primers
550 CGTTTAAACTACAGTTCCATTGGAGCAAC and TAGGTACCTGCGATCTAACAATTT
551 CAGACTTC. The tdTomato gene was amplified from a donor vector[77] with primers
552 CAGGTACCATGGTGAGCAAGGGCGAGGAGGT and TGGCGCGCCCTT
553 GTACAGCTCCTCCATGCCGT. The 35S promoter of pMDC43 was exchanged with the
554 *KEULE* upstream regulatory region via PmeI and Acc65I sites, and GFP in pMDC43 was
555 exchanged with *tdTomato* via KpnI and AscI sites. The full-length *KEULE* gene was amplified
556 from genomic DNA using primers GGGGACAAGTTTGTACAAAAAAGCAG
557 GCTTGACCATGTCGTACTCTGACTCC and GGGGACCACTTTGTACAAGAAAGCTGGG
558 TTTATTTGGAGATCGTCTA and then inserted into the modified pMDC43 vector using
559 Gateway cloning technology (Invitrogen) as described previously[78]. The construct was
560 introduced into plants heterozygous for the keulemm125 deletion mutation[79] via Agrobacterium-
561 mediated transformation[80,81]. T2 plants were genotyped for the *KEULE* locus using PCR: primers
562 CGACCTTATCAGAGAGCAAGG and Keu-as0 (ACAGGGATTTGATTTGAGATCTGG)
563 amplified a 1661-bp fragment from the wild-type allele and a 1505-bp allele from the deletion
564 allele. Additionally, the primer pair GTCTGTTAACGGCTGCAGAA and Keu-as0 was used to
565 amplify a fragment (1103 bp) only present in the wild-type allele. A T2 plant homozygous for
566 the deletion allele and hemizygous for the *pKEULE-tdTomato-KEULE* transgene was isolated.
567 A doubly homozygous line was subsequently isolated in the T3 generation and used for
568 experiments.

569 To generate double-labeled plants expressing markers for KEULE protein and cellulose
570 synthase, homozygous *pKEULE-tdTomato-KEULE/ keulemm125* plants (ecotype Landsberg)
571 were crossed with homozygous *pCESA6-Citrine-CESA6/cesa6prc1-1* plants (ecotype
572 Columbia[53]. An F2 line was selected that was homozygous for both mutations and hemizygous
573 for both markers. In the F3 generation, a quadruply homozygous plant was isolated together
574 with a plant homozygous for both mutations, homozygous for *pCESA6-Citrine-CESA6* and
575 hemizygous for *pKEULE-tdTomato-KEULE*. Seed from the latter plant thus show segregation
576 for the *keule* mutant phenotype.

577 To generate double-labeled plants expressing markers for KEULE protein and
578 microtubules, *p35S-EGFP-TUA5* was introduced into *pKEULE-tdTomato-KEULE/keulemm125*
579 plants via Agrobacterium-mediated transformation. T2 seedlings expressing the microtubule
580 label were used for experiments.

581

582 Growth

583 Seedlings were grown in the dark on vertical agar plates as described in Lindeboom et al.[69].
584 For hypocotyl elongation assays, seedlings were grown for 5 days. For live cell imaging
585 experiments, seedlings were imaged 3 days after germination.

586

587 Drug treatments

588 Oryzalin, taxol and isoxaben were dissolved in DMSO for 100x stock solutions. Oryzalin
589 was used at a final concentration of 20 µM, taxol (Sigma) at 20 µM and isoxaben (Sigma) at 100
590 nM in plant growth media (Hoagland's No. 2). Mannitol was dissolved in plant growth media

591 directly at a concentration of 200 mM. For control treatment (mock), DMSO was added to the
592 growth media to a final concentration of 0.01%. Incubation of the seedlings was performed in 6-
593 well plates (WVR, nontreated) with 2 mL of plant growth media in each well. The plates were
594 wrapped in aluminum foil to block light and incubated at 22 °C. The drug treatment durations
595 were 16 hours for oryzalin, and 2 hours for all other treatments. Likewise, the mock treatments
596 were 16 hours for comparison to oryzalin, and 2 hours for comparison to the remaining
597 treatments.
598
599 Confocal microscopy
600 Imaging was performed on an instrument featuring a CSU-X1 spinning disk head
601 (Yokogawa Electric), a DMI6000 B inverted microscope (Leica), a 100X/1.4 NA oil immersion
602 objective (Leica), an Evolve 512 EMCCD camera (Photometrics) and a 1.2X telescope between
603 the spinning disk unit and camera. EGFP/CITRINE and tdTomato were excited at 488 nm and
604 561 nm respectively, by solid-state lasers (Coherent Cube). Switching, shuttering and intensity of
605 these lasers was performed by direct electronic control. Emission filtering was accomplished
606 with bandpass filters, (525/50 nm for EGFP and CITRINE and 636/37 nm for tdTomato
607 (SemRock), together with a 405/488/568 nm dichroic filter (SemRock). Exposure times were
608 400 ms for tdTomato-KEULE, 200 ms for EGFP-TUA5 and 800 ms for Citrine-CESA6. Images
609 were acquired at 1 second intervals in experiments in which both tdTomato-KEULE and EGFP-
610 TUA5 were imaged and 2 second intervals in experiments featuring tdTomato-KEULE together
611 with Citrine-CESA6. All light energies were approximately 4 mW as measured at the end of the
612 optical fiber entering the confocal head. For high-speed acquisitions of tdTomato-KEULE,
613 image streaming was performed at an acquisition rate of 5 Hz (200 ms exposures). The focal
614 plane in all experiments was stabilized by hardware Adaptive Focus Control (Leica) to mitigate
615 changes in specimen intensity over time caused by thermal and mechanical drift in focus.
616 Photobleaching was performed by a Vector laser scanning unit (Intelligent Imaging
617 Innovations) integrated into the setup above at the right camera port. Focused laser light was
618 pulsed and scanned (pulse duration = 10 ms, raster block size = 20 units) on the image plane by a
619 pair of galvanometer-driven mirrors inside the Vector unit. Scanner positions were calibrated to
620 image coordinates using an automated procedure in Slidebook software (Intelligent Imaging
621 Innovations). Citrine photobleaching was performed using the 488 nm laser at the same power as
622 used for imaging but focused on the image plane. Areas of ~200 μm^2 were bleached in 20-30 s.
623 All imaging was performed on the upper hypocotyl cells (1-2 mm below the apical hook).
624 Specimen mounting was performed as described previously[69].
625
626 Image registration
627 To correct for lateral specimen drift in the movies, we performed image registration in
628 MATLAB. We first performed a running average on the image sequence using a three frame
629 window (yielding an image series 2 frames shorter than the original series). We then performed
630 an intensity-based image registration algorithm using the MATLAB function imregtform, using
631 tformtype "translation" and conserving the pixel size. To minimize interpolation artifacts, we
632 first determined the transformation matrix that yielded the best intensity match for each
633 consecutive image pair, then calculated the cumulative transformation matrix for the whole
634 averaged image series and applied it to the original movie that was not frame averaged, minus
635 the first and last frame that were lost because of the frame averaging. Some of the KEULE-
636 tdTomato and Citrine-CESA colocalization movies (3 out of 8) still exhibited sample drift after

intensity-based registration. In those cases, we applied a feature-based method employing the locations of detected KEULE spots (See Methods: Particle Tracking for details) as registration features and using the MATLAB function estgeotform2d and a rigid transform.

KEULE particle tracking, streaming experiments, image series with labeled microtubules

Particle detection and tracking was performed on the registered movies. For streaming experiments and experiments featuring labeled microtubules (1 second time intervals) we used µTrack[49] to detect and estimate the positions of tdTomato-KEULE clusters in each frame and subsequently link detected foci from frame to frame to track individual KEULE clusters over time. For each experiment type, we used the following parameters:

Streaming image series.

For detection: initial psfSigma = 1.2 pixels, alpha for local max 0.05 and 10 max iterations for psfSigma estimation.

For tracking: max detection gap = 2 frames, min track length = 4 frames, max search radius = 2 pixels, gap penalty = 4.

1-second interval image series.

For detection: initial psfSigma = 1.2 pixels, alpha for local max 0.05 and 10 max iterations for psfSigma estimation.

For tracking: max detection gap = 1 frame, min track length = 1 frames, max search radius = 3 pixels, gap penalty = 4.

KEULE and CESA particle tracking in dual labeled movies

In experiments assessing KEULE localization and dynamics with respect to cellulose synthase complex (CSC) trafficking and we used the Spots module in Imaris software (Bitplane) to detect and track both tdTomato-KEULE clusters and Citrine-CESA6 particles. The Imaris Spots detector and filters performed better for Citrine-CESA6 signals, in particular. CSCs as labeled by Citrine-CESA6 were detected using a size value of 0.3 µm and quality value of 110. Tracking was performed by applying the Autoregressive Motion algorithm (maximum distance = 0.35 µm, maximum gap size = 2 frames). Successful deliveries of CSC complexes to the plasma membrane were determined by dynamic criteria as described previously[7]. Briefly, a delivery event was defined when puncta that were mobile in the streaming cytosol (1) stabilized positionally in the optical plane of the plasma membrane, and (2) showed a transition to slow, steady and linear movement in the velocity range (~200-450 nm/min) we previously have determined be characteristic of CSC's actively synthesizing and extruding cellulose fibers into the cell wall[53]. To make this assessment, we first filtered CSC tracks by duration (>30 seconds), then used a custom GUI in MATLAB to manually inspect and verify each Spots track and associated image data for these characteristics. As a part of this process, the frame in which a tracked particle first showed evidence of stabilized lateral position was marked as the "tethering" frame – the frame showing the time and location of first stable interaction with the cell cortex of a presumed vesicle carrying one or more labeled CSC's.

Clusters of tdTomato-KEULE were detected with Spots module using a size parameter value of 0.3 µm, a quality value of 100 and were tracked using the Connected Components algorithm (frame to frame displacements of KEULE signal are small and not auto-correlated).

These settings adequately detected and tracked KEULE clusters based on visual inspection of the results.

Maximum Likelihood Gaussian fitting for particles

We employed maximum likelihood Gaussian fitting as described in Mortensen et al.[50] to use photon counts in estimating the accuracy of particle position and shape. To determine the number of photons collected in each image pixel, we first needed to calibrate our camera gain (photoelectrons per grey value or ADU). Photon detection can be modeled as a Poisson process, which creates a distribution in which the mean equals the variance. Therefore, the camera gain is equal to the coefficient between the mean and variance of the gray values in the image. To calculate this coefficient, we first measured the noise floor of the camera by taking the average of the gray values (intensity) of images acquired with the camera capped. We then determined the grey value variance by subtracting one image from the other then calculating the variance among these pixel-by-pixel difference values. To obtain the final variance, we divided this number by 2 to account for the fact we are using two images for determining the differences. Finally, we calculated the mean intensity of the images, subtracted the noise floor, and divided by the variance to estimate the camera gain.

For each time point in every track, we cropped out a pixel grid with the estimated center of the detected KEULE spot in the middle pixel (9 x 9 pixels). Along with a cropped image, the fitting routine requires a set of initial parameters: xCoordinate, yCoordinate, point spread function standard deviation (PSF SD), background, and an estimate of number of photons that comprise the imaged PSF. The x- and y-coordinates we used are the estimates of position from the particle tracking described above. Based on the approximate emission wavelength and objective numerical aperture, we used 133 nm for the initial standard deviation of the PSF. We estimated the background by calculating the median intensity of the outer border of the pixel grid used for fitting after subtraction of the camera noise floor. If the center of the point source is in the middle of the pixel and the PSF SD is 133 nm, we expect 0.16 of the photoelectrons to be in the center pixel. Therefore, we estimated the number of photoelectrons in the imaged spot by first subtracting the noise floor and pixel background from the intensity in the center pixel and multiplying the result by 1/0.16 (6.25). Before performing fitting using these initial data, we needed to address noise that could have been introduced by bilinear interpolation during the image registration that was employed to mitigate specimen drift. To accomplish this, we used the transformation matrix from registration to map the locations of the tracked particles back to the locations in the original image sequence, we then performed MLE fitting on the non-interpolated images by employing the method of Mortenson et al. [50] in MATLAB.

Since we used free fit parameters and there is noise in the data from photon counting, free fluorescently tagged proteins, high local particle densities and unresolved distributions of labeled structures, we excluded distance measurement from fits that were outside the expected parameter ranges. In the case of the SD of the 2D Gaussian, we found that there was a distinct population where the SD fit parameter was < 50 nm. Since our pixels correspond to 133 nm, in these fits all the photoelectrons are contained in one pixel, which is not consistent for a diffraction-limited spot at the magnification onto our camera (roughly 4 pixels). Similarly, we found that fit SD values above 2x the estimated PSF SD in most cases represented a fit containing more than one particle. Therefore, SD fit results with SD values outside 50 to 266 nm were excluded from position measurements. Fit results with estimated numbers of photoelectrons > 1000 were also considered outliers and excluded. Finally, high local particle densities the distance in some cases

caused the MLEwG fit to center on a nearby particle and not the particle marked by the starting position. We therefore also did not include position information for fits where the distance between the original estimate and the MLEwG position differed more than 2 x 133 nm. See Fig. S6 for fit parameters for the tdTomato-KEULE clusters and CIT-CESA6 labeled CSCs.

KEULE to microtubule distance measurements

To determine the position of each KEULE spot to assess the spatial relationship of KEULE accumulation with the microtubule cytoskeleton we first determined the single frame with the highest number of measured photoelectrons for each KEULE track. For tracks that were longer than 4 frames we determined the max number of photoelectrons using a running three frames average, for shorter tracks we did not use frame averaging. The rational for this selection was two-fold. First, we reasoned that maximum signal might best be associated with the site of KEULE function, with initial signal rise being indicative of KEULE recruitment and/or assembly into a membrane fusion structure, and signal loss indicating KEULE disassociation or disassembly of the fusion machinery. Second, the precision of estimated position is proportional to photon sampling. It is also relevant to note that frame-to-frame movement of KEULE tracks were small (Fig. S7).

To locate positions of microtubule signal relative to each KEULE track location, we used a rotating linear filter combined with analysis of signal peaks and a two-step fitting procedure. At the coordinates of KEULE signal in each max value frame we drew a line 21 pixels long and 1 pixel wide extending 10.5 pixels to each side of the KEULE position and repeated this process in increments of 9 degrees to cover 360 degrees (Fig. 4C). We then projected this array of lines on the microtubule channel and extracted the intensities (in photons) along each line at 1-pixel (133 nm) intervals by bilinear interpolation. To locate potential positions of microtubule signal along each sampling angle we used the MATLAB function Findpeaks with a MinPeakProminence of 25 to identify signal peaks. The 10.5-pixel distance is typically long enough to contain the peak intensity of the nearest microtubule. In fact, in many cases this length intersects multiple microtubules, but it is also possible for the end of the lines to partially intersect a microtubule with a peak outside the 10.5 pixels. For subsequent fitting steps, we included pixels from the center until the furthest peak on each side plus 3 pixels to catch the shoulder of these peaks, and at the same time, exclude signal from microtubules whose peaks are just outside the 10.5 pixel range from influencing the fitting. We then estimated the center position of each signal peak by modifying the 2D MLEwG[50] to a quasi-1D version, modeling the microtubule as a Gaussian wall[82] that is one pixel wide, as shown in the formula below.

(Formula 1)

$$\mathrm{N}\left(\frac{1}{\sqrt{2\pi\sigma^2}}\right)\left(\frac{1}{a}\right)\exp\left(-\frac{(x-\mu_x)^2}{2\sigma^2}\right)+b^2$$

Where:

N = number of photoelectrons

σ = Standard deviation

a = nm per pixel

x = position on the line

μ_x = center position

b = background photoelectrons

We found up to four peaks on a single line and fitted all peaks simultaneously by adding an additional term describing each additional peak as follows:

(Formula 2)

$$N_{\text{first}}\left(\frac{1}{\sqrt{2\pi\sigma_{\text{first}}^2}}\right)\left(\frac{1}{a}\right)\exp\left(-\frac{(x-\mu_{x\ \text{first}})^2}{2\sigma_{\text{first}}^2}\right)+$$

(Formula 3)

$$N_{\text{second}}\left(\frac{1}{\sqrt{2\pi\sigma_{\text{second}}^2}}\right)\left(\frac{1}{a}\right)\exp\left(-\frac{(x-\mu_{x\ \text{second}})^2}{2\sigma_{\text{second}}^2}\right)+b_{\text{global}}^2$$

For estimating the seeding parameters for the fit, we used the center of the maximum value pixel for each peak identified by Findpeaks. We used 160 nm (median value of the peak population) as the estimate for the standard deviation and we approximated the background by taking the square root of the lowest 10 percentile of all the pixels for all angles after subtracting the noise floor.

After fitting all microtubule peaks along all angular steps, we determined the distance from the KEULE location to the center of the nearest microtubule signal. We did this in three steps. First, we determined the nearest microtubule signal peak to the KEULE location from among the initial angular samples. Second, we determined the angle of the microtubule identified by the closest peak. Measuring the distance from the KEULE location to the center of the microtubule signal is most accurate along a line perpendicular from the KEULE location to the microtubule. By determining the local microtubule signal angle, we could then determine the optimal perpendicular sample angle. To find the local orientation of the microtubule we rotated a line of 21 pixels long around the center of the location where we initially found the closest microtubule peak. We extracted the summed signal intensities along these lines and determined the angle at which we found the maximum intensity, corresponding to the microtubule angle[69]. Finally, once we established the microtubule angle, we used the angle perpendicular to that microtubule angle to extract the nearest microtubule fit for the representative KEULE position. Distance values where the fit parameters for the microtubule positions were the number of photoelectrons were < 50 or > 10000, as well as SD fit parameters < 50 or > 250 nm were excluded from distance measurements. We required all the microtubule fits on the line to be within these parameters to be included in the analysis. See Fig. S8A-C for fit parameters for KEULE (A) and microtubule signal (B) fits after selection as well as the standard error of the distance measurement between them (C).

<u>Analysis of KEULE localization with CESA6 delivery sites</u>

KEULE and CESA6 spots were detected and tracked in Imaris as described above and maximum likelihood 2D Gaussian fitting was applied to each set of tracks. CESA tracks tend to

be relatively long and can be confounded by a dynamic background produced by highly motile CESA containing organelles including Golgi bodies and Trans-Golgi network compartments. This background makes fully automated detection and quantitation of CSC delivery events challenging. We therefore designed a graphical user interface in MATLAB that allowed us to efficiently curate potential CESA delivery events identified in Imaris and verify whether individual tracks were indeed depicting a CESA delivery. We have shown previously that CESA delivery to the plasma membrane typically shows three distinct phases; (1) erratic movement of CESA containing vesicles as they appear in the optical plane at the cell cortex, (2) positional-stabilization and (3) slow and steady movement with typically linear trajectories. We speculate that the second phase represents molecular tethering at the plasma membrane and the events that lead to vesicle fusion and cargo delivery. The third phase is behavior that we have shown is characteristic of active CSC complexes in the plasma membrane as they synthesize cellulose[53]. Thus, observation of this latter behavior indicates successful delivery of CESA cargo to the plasma membrane. For each CESA track that showed these three distinct phases, we marked the first frame of CESA stabilization at the plasma membrane. From this position, we determined the distance to the nearest KEULE spot in a 30-frame time range (60 seconds). Some degree of coincidence between CESA deliveries and KEULE spots is expected by chance alone, especially since the density of KEULE clusters at the plasma membrane is relatively high. To evaluate whether the observed distribution of KEULE locations with sites of CESA stabilization might be due to chance alone, we generated random positions in the same regions of interest used for the experimental data and calculated the distances to the nearest KEULE spot. We used these simulated data to model the expected distribution of distances and compared this distribution to the distribution of distances found for confirmed CESA delivery events. First, we divided both the experimental and simulated distance distributions up into 40 nm distance bins and calculated the bin-by-bin count frequencies by the total number of simulated counts. We then introduced a bias parameter δ that equates an observed frequency in each distance bin to the expected value from the simulated distribution as shown in formula (4).

(Formula 4)

$$P_{inDistBin}(\delta) = \frac{\text{Expected}_{inDistBin}\,\delta}{Expected_{\text{inDistBin}}\,\delta + \text{Expected}_{\text{outsideDistBin}}(1-\delta)}$$

The value of δ may vary between 0 and 1. For a possible observed frequency that equals the expected frequency, δ is equal 0.5. If δ is greater than 0.5, an observed frequency is higher than expected. Likewise, if δ is less than 0.5 the observed frequency lower than expected under the null hypothesis. Use of the parameter allows us to use a Bayesian approach to test multiple hypotheses to ask what bias value best may best explain the actual observed frequencies. To do this, we calculated the Likelihood Ratio of observing an experimental result given a range of values for δ (in increments of 0.001, excluding 0) for each frequency bin:

(Formula 5)

$$\frac{L(\delta)}{L\frac{1}{2}} = \frac{P_{inDistBin}\,(\delta)^{M}\,(1\,-\,P_{inDistBin}\,(\delta)^{N-M})}{Expected^{N}_{inDistBin}\,Expected^{N-M}_{outsideDistBin}}$$

Where:

$L(\delta)$ = likelihood of the data given the bias δ,

$L\frac{1}{2}$ = likelihood of the data in the neutral case (no positive or negative bias)
N = total number of measurements
M = number of measurements in this specific distance bin

We then found the maximum a posteriori probability (MAP) for δ and computed the shortest range of δ values for the highest posterior density (HPD) that contains 95% of the normalized probability density. Maximum likelihood estimates for δ below 0.5 indicate underrepresentation at the distance of interest and above 0.5 indicate overrepresentation of experimental data compared to the unbiased case.

Analysis of KEULE localization with microtubules

We used the same Bayesian approach describe above for analyzing the localization of KEULE clusters with respect to the estimated center of the nearest microtubule. We changed the distance bin size from 40 to 20 nm.

Hot spot analysis

To investigate if some KEULE events are independent of each other each or not (e.g. if "hot spots" for KEULE accumulation may exist), we examined colocalization between sequential KEULE spots in time series collected from cells expressing both labeled KEULE and tubulin proteins. Within a region of interest in each time series, we selected all KEULE tracks that were first detected between frames 2 and 31 and calculated the distance to all other KEULE tracks that started subsequently up to and including frame 301. For position estimates we used the frame in the track that showed the highest number of fitted photoelectrons. To compare the degree of colocalization of the initial KEULE tracks with future KEULE tracks to that expected from chance alone, we created a simulated initial dataset with random locations within the same region of interest and calculated the distances to all KEULE tracks in the same time range.

Since KEULE foci are positionally stable we chose a stringent distance threshold of 133 nm (1 pixel) to declare two spots or locations to be co-localized. Because of the relatively high density of KEULE spots at the plasma membrane, colocalization is expected at some point in time, therefore the time frame of colocalization analysis is also important. Indeed, we observe a large degree of colocalization in the whole dataset for both the experimental and simulated data, but with very distinct waiting time distributions (Fig. S5D). Based on the differences in the distribution of waiting times between random simulated positions and KEULE positions until the next KEULE spot arrives, we determined that a 40 second time delay window captures most biologically relevant colocalizations while excluding most random colocalizations due to KEULE density and chance.

894

895 1. Noordstra, I., and Akhmanova, A. (2017). Linking cortical microtubule attachment and
896 exocytosis. F1000Research *6*, 469. https://doi.org/10.12688/f1000research.10729.1.

897 2. Spiliotis, E.T., and Nelson, W.J. (2003). Spatial control of exocytosis. Curr. Opin. Cell Biol.
898 *15*, 430–437. https://doi.org/10.1016/s0955-0674(03)00074-7.

899 3. Fourriere, L., Jimenez, A.J., Perez, F., and Boncompain, G. (2020). The role of microtubules
900 in protein transport. Journal of Cell Science *133*, jcs237016. https://doi.org/10.1242/jcs.237016.

901 4. Chang, F., and Martin, S.G. (2009). Shaping Fission Yeast with Microtubules. Cold Spring
902 Harb. Perspect. Biol. *1*, a001347. https://doi.org/10.1101/cshperspect.a001347.

903 5. Bartolini, F., and Gundersen, G.G. (2006). Generation of noncentrosomal microtubule arrays.
904 J. Cell Sci. *119*, 4155–4163. https://doi.org/10.1242/jcs.03227.

905 6. Shaw, S.L., Kamyar, R., and Ehrhardt, D.W. (2003). Sustained Microtubule Treadmilling in
906 Arabidopsis Cortical Arrays. Science *300*, 1715–1718. https://doi.org/10.1126/science.1083529.

907 7. Gutierrez, R., Lindeboom, J.J., Paredez, A.R., Emons, A.M.C., and Ehrhardt, D.W. (2009).
908 Arabidopsis cortical microtubules position cellulose synthase delivery to the plasma membrane
909 and interact with cellulose synthase trafficking compartments. Nat. Cell Biol. *11*, 797–806.
910 https://doi.org/10.1038/ncb1886.

911 8. Sampathkumar, A., Gutierrez, R., McFarlane, H.E., Bringmann, M., Lindeboom, J., Emons,
912 A.-M., Samuels, L., Ketelaar, T., Ehrhardt, D.W., and Persson, S. (2013). Patterning and
913 Lifetime of Plasma Membrane-Localized Cellulose Synthase Is Dependent on Actin
914 Organization in Arabidopsis Interphase Cells. Plant Physiol. *162*, 675–688.
915 https://doi.org/10.1104/pp.113.215277.

916 9. Vellosillo, T., Dinneny, J.R., Somerville, C.R., and Ehrhardt, D.W. (2021). TRANVIA (TVA)
917 facilitates cellulose synthase trafficking and delivery to the plasma membrane. Proc. Natl. Acad.
918 Sci. *118*, e2021790118. https://doi.org/10.1073/pnas.2021790118.

919 10. Gutierrez, R., Lindeboom, J.J., Paredez, A.R., Emons, A.M.C., and Ehrhardt, D.W. (2009).
920 Arabidopsis cortical microtubules position cellulose synthase delivery to the plasma membrane
921 and interact with cellulose synthase trafficking compartments. Nature Cell Biology *11*, 797–806.
922 https://doi.org/10.1038/ncb1886.

923 11. Li, S., Lei, L., Somerville, C.R., and Gu, Y. (2012). Cellulose synthase interactive protein 1
924 (CSI1) links microtubules and cellulose synthase complexes. Proc. Natl. Acad. Sci. *109*, 185–
925 190. https://doi.org/10.1073/pnas.1118560109.

926 12. Bringmann, M., Li, E., Sampathkumar, A., Kocabek, T., Hauser, M.-T., and Persson, S.
927 (2012). POM-POM2/CELLULOSE SYNTHASE INTERACTING1 Is Essential for the

928 Functional Association of Cellulose Synthase and Microtubules in Arabidopsis. Plant Cell *24*,
929 163–177. https://doi.org/10.1105/tpc.111.093575.

930 13. Zhu, X., Li, S., Pan, S., Xin, X., and Gu, Y. (2018). CSI1, PATROL1, and exocyst complex
931 cooperate in delivery of cellulose synthase complexes to the plasma membrane. Proc. Natl.
932 Acad. Sci. *115*, E3578–E3587. https://doi.org/10.1073/pnas.1800182115.

933 14. Lei, L., Singh, A., Bashline, L., Li, S., Yingling, Y.G., and Gu, Y. (2015). CELLULOSE
934 SYNTHASE INTERACTIVE1 Is Required for Fast Recycling of Cellulose Synthase Complexes
935 to the Plasma Membrane in Arabidopsis. The Plant Cell *27*, 2926–2940.
936 https://doi.org/10.1105/tpc.15.00442.

937 15. Paredez, A.R., Somerville, C.R., and Ehrhardt, D.W. (2006). Visualization of Cellulose
938 Synthase Demonstrates Functional Association with Microtubules. Science *312*, 1491–1495.
939 https://doi.org/10.1126/science.1126551.

940 16. Gutierrez, R., Lindeboom, J.J., Paredez, A.R., Emons, A.M.C., and Ehrhardt, D.W. (2009).
941 Arabidopsis cortical microtubules position cellulose synthase delivery to the plasma membrane
942 and interact with cellulose synthase trafficking compartments. Nature Cell Biology *11*, 797–806.
943 https://doi.org/10.1038/ncb1886.

944 17. DeBolt, S., Gutierrez, R., Ehrhardt, D.W., Melo, C.V., Ross, L., Cutler, S.R., Somerville, C.,
945 and Bonetta, D. (2007). Morlin, an inhibitor of cortical microtubule dynamics and cellulose
946 synthase movement. Proc. Natl. Acad. Sci. *104*, 5854–5859.
947 https://doi.org/10.1073/pnas.0700789104.

948 18. Emons, A.M.C., Mulder, B.M., Emons, A.M.C., and Mulder, B.M. (2000). How the
949 deposition of cellulose microfibrils builds cell wall architecture. Trends Plant Sci. *5*, 35–40.
950 https://doi.org/10.1016/s1360-1385(99)01507-1.

951 19. Hamant, O., Heisler, M.G., Jönsson, H., Krupinski, P., Uyttewaal, M., Bokov, P., Corson, F.,
952 Sahlin, P., Boudaoud, A., Meyerowitz, E.M., et al. (2008). Developmental Patterning by
953 Mechanical Signals in Arabidopsis. Science *322*, 1650–1655.
954 https://doi.org/10.1126/science.1165594.

955 20. Zhang, B., Karnik, R., Alvim, J., Donald, N., and Blatt, M.R. (2019). Dual Sites for SEC11
956 on the SNARE SYP121 Implicate a Binding Exchange during Traffic1. Plant Physiol *180*, 228–
957 239. https://doi.org/10.1104/pp.18.01315.

958 21. Honsbein, A., Sokolovski, S., Grefen, C., Campanoni, P., Pratelli, R., Paneque, M., Chen, Z.,
959 Johansson, I., and Blatt, M.R. (2009). A tripartite SNARE-K+ channel complex mediates in
960 channel-dependent K+ nutrition in Arabidopsis. Plant Cell *21*, 2859–2877.
961 https://doi.org/10.1105/tpc.109.066118.

962 22. Assaad, F.F., Qiu, J.-L., Youngs, H., Ehrhardt, D., Zimmerli, L., Kalde, M., Wanner, G.,
963 Peck, S.C., Edwards, H., Ramonell, K., et al. (2004). The PEN1 Syntaxin Defines a Novel

964 Cellular Compartment upon Fungal Attack and Is Required for the Timely Assembly of Papillae.
965 Mol. Biol. Cell *15*, 5118–5129. https://doi.org/10.1091/mbc.e04-02-0140.

966 23. Bloch, D., Pleskot, R., Pejchar, P., Potocký, M., Trpko¡ová, P., Cwiklik, L., Vuka¡inović, N.,
967 Sternberg, H., Yalovsky, S., and Žárský, V. (2016). Exocyst SEC3 and Phosphoinositides Define
968 Sites of Exocytosis in Pollen Tube Initiation and Growth. Plant Physiol. *172*, 980–1002.
969 https://doi.org/10.1104/pp.16.00690.

970 24. Fendrych, M., Synek, L., Pečenková, T., Drdová, E.J., Sekereš, J., Rycke, R. de, Nowack,
971 M.K., and Žárský, V. (2013). Visualization of the exocyst complex dynamics at the plasma
972 membrane of Arabidopsis thaliana. MBoC *24*, 510–520. https://doi.org/10.1091/mbc.e12-06-
973 0492.

974 25. Barg, S., Knowles, M.K., Chen, X., Midorikawa, M., and Almers, W. (2010). Syntaxin
975 clusters assemble reversibly at sites of granules in live cells. Proceedings of the National
976 Academy of Sciences *107*, 20804–20809. https://doi.org/10.1073/pnas.1014823107.

977 26. Knowles, M.K., Barg, S., Wan, L., Midorikawa, M., Chen, X., and Almers, W. (2010).
978 Single granules of live cells recruit syntaxin-1 and synaptosomal associated protein 25 (SNAP-
979 25) in large copy numbers. Proceedings of the National Academy of Sciences *107*, 20810–
980 20815. https://doi.org/10.1073/pnas.1014840107.

981 27. McNew, J.A., Weber, T., Parlati, F., Johnston, R.J., Melia, T.J., Söllner, T.H., and Rothman,
982 J.E. (2000). Close Is Not Enough. The Journal of Cell Biology *150*, 105–118.
983 https://doi.org/10.1083/jcb.150.1.105.

984 28. Südhof, T.C., and Rothman, J.E. (2009). Membrane Fusion: Grappling with SNARE and SM
985 Proteins. Science *323*, 474–477. https://doi.org/10.1126/science.1161748.

986 29. Burgoyne, R.D., Barclay, J.W., Ciufo, L.F., Graham, M.E., Handley, M.T.W., and Morgan,
987 A. (2009). The Functions of Munc18-1 in Regulated Exocytosis. Ann. N. York Acad. Sci. *1152*,
988 76–86. https://doi.org/10.1111/j.1749-6632.2008.03987.x.

989 30. Baker, R.W., Jeffrey, P.D., Zick, M., Phillips, B.P., Wickner, W.T., and Hughson, F.M.
990 (2015). A direct role for the Sec1/Munc18-family protein Vps33 as a template for SNARE
991 assembly. Science *349*, 1111–1114. https://doi.org/10.1126/science.aac7906.

992 31. Stepien, K.P., Prinslow, E.A., and Rizo, J. (2019). Munc18-1 is crucial to overcome the
993 inhibition of synaptic vesicle fusion by αSNAP. Nat. Commun. *10*, 4326.
994 https://doi.org/10.1038/s41467-019-12188-4.

995 32. Peng, R.-W., Guetg, C., Abellan, E., and Fussenegger, M. (2010). Munc18b regulates core
996 SNARE complex assembly and constitutive exocytosis by interacting with the N-peptide and the
997 closed-conformation C-terminus of syntaxin 3. Biochem. J. *431*, 353–361.
998 https://doi.org/10.1042/bj20100145.

999 33. Hashizume, K., Cheng, Y.-S., Hutton, J.L., Chiu, C., and Carr, C.M. (2009). Yeast Sec1p
1000 Functions before and after Vesicle Docking. Mol. Biol. Cell *20*, 4673–4685.
1001 https://doi.org/10.1091/mbc.e09-02-0172.

1002 34. Mayer, U., Ruiz, R.A.T., Berleth, T., Miséra, S., and Jürgens, G. (1991). Mutations affecting
1003 body organization in the Arabidopsis embryo. Nature *353*, 402–407.
1004 https://doi.org/10.1038/353402a0.

1005 35. Assaad, F.F., Mayer, U., Wanner, G., and Jürgens, G. (1996). The KEULE gene is involved
1006 in cytokinesis in Arabidopsis. Mol. Gen. Genet. MGG *253*, 267–277.
1007 https://doi.org/10.1007/pl00008594.

1008 36. Karnik, R., Grefen, C., Bayne, R., Honsbein, A., Köhler, T., Kioumourtzoglou, D., Williams,
1009 M., Bryant, N.J., and Blatt, M.R. (2013). Arabidopsis Sec1/Munc18 protein SEC11 is a
1010 competitive and dynamic modulator of SNARE binding and SYP121-dependent vesicle traffic.
1011 Plant Cell *25*, 1368–1382. https://doi.org/10.1105/tpc.112.108506.

1012 37. Karnik, R., Zhang, B., Waghmare, S., Aderhold, C., Grefen, C., and Blatt, M.R. (2015).
1013 Binding of SEC11 indicates its role in SNARE recycling after vesicle fusion and identifies two
1014 pathways for vesicular traffic to the plasma membrane. Plant Cell *27*, 675–694.
1015 https://doi.org/10.1105/tpc.114.134429.

1016 38. Karnahl, M., Park, M., Krause, C., Hiller, U., Mayer, U., Stierhof, Y.-D., and Jürgens, G.
1017 (2018). Functional diversification of Arabidopsis SEC1-related SM proteins in cytokinetic and
1018 membrane fusion. Proceedings of the National Academy of Sciences *115*, 6309–6314.
1019 https://doi.org/10.1073/pnas.1722611115.

1020 39. Assaad, F.F., Huet, Y., Mayer, U., and Jürgens, G. (2001). The Cytokinesis Gene KEULE
1021 Encodes a Sec1 Protein That Binds the Syntaxin Knolle. The Journal of Cell Biology *152*, 531–
1022 544. https://doi.org/10.1083/jcb.152.3.531.

1023 40. Assaad, F.F., Mayer, U., Wanner, G., and Jürgens, G. (1996). The KEULE gene is involved
1024 in cytokinesis in Arabidopsis. Molecular and General Genetics MGG *253*, 267–277.
1025 https://doi.org/10.1007/pl00008594.

1026 41. Carr, C.M., Grote, E., Munson, M., Hughson, F.M., and Novick, P.J. (1999). Sec1p Binds to
1027 SNARE Complexes and Concentrates at Sites of Secretion. J. Cell Biol. *146*, 333–344.
1028 https://doi.org/10.1083/jcb.146.2.333.

1029 42. Scott, B.L., Komen, J.S.V., Irshad, H., Liu, S., Wilson, K.A., and McNew, J.A. (2004).
1030 Sec1p directly stimulates SNARE-mediated membrane fusion in vitro. J. Cell Biol. *167*, 75–85.
1031 https://doi.org/10.1083/jcb.200405018.

1032 43. Zilly, F.E., Sørensen, J.B., Jahn, R., and Lang, T. (2006). Munc18-Bound Syntaxin Readily
1033 Forms SNARE Complexes with Synaptobrevin in Native Plasma Membranes. PLoS Biol. *4*,
1034 e330. https://doi.org/10.1371/journal.pbio.0040330.

1035 44. Medine, C.N., Rickman, C., Chamberlain, L.H., and Duncan, R.R. (2007). Munc18-1
1036 prevents the formation of ectopic SNARE complexes in living cells. J. Cell Sci. *120*, 4407–4415.
1037 https://doi.org/10.1242/jcs.020230.

1038 45. Rickman, C., and Duncan, R.R. (2010). Munc18/Syntaxin Interaction Kinetics Control
1039 Vesicle Dynamics2. J. Biol. Chem. *285*, 3965–3972. https://doi.org/10.1074/jbc.m109.040402.

1040 46. Smyth, A.M., Rickman, C., and Duncan, R.R. (2010). Vesicle Fusion Probability Is
1041 Determined by the Specific Interactions of Munc18*. J. Biol. Chem. *285*, 38141–38148.
1042 https://doi.org/10.1074/jbc.m110.164038.

1043 47. Trexler, A.J., Sochacki, K.A., and Taraska, J.W. (2016). Imaging the recruitment and loss of
1044 proteins and lipids at single sites of calcium-triggered exocytosis. Mol. Biol. Cell *27*, 2423–2434.
1045 https://doi.org/10.1091/mbc.e16-01-0057.

1046 48. Somasundaram, A., and Taraska, J.W. (2018). Local protein dynamics during microvesicle
1047 exocytosis in neuroendocrine cells. Mol. Biol. Cell *29*, 1891–1903.
1048 https://doi.org/10.1091/mbc.e17-12-0716.

1049 49. Jaqaman, K., Loerke, D., Mettlen, M., Kuwata, H., Grinstein, S., Schmid, S.L., and Danuser,
1050 G. (2008). Robust single-particle tracking in live-cell time-lapse sequences. Nat. Methods *5*,
1051 695–702. https://doi.org/10.1038/nmeth.1237.

1052 50. Mortensen, K.I., Churchman, L.S., Spudich, J.A., and Flyvbjerg, H. (2010). Optimized
1053 localization analysis for single-molecule tracking and super-resolution microscopy. Nat.
1054 Methods *7*, 377–381. https://doi.org/10.1038/nmeth.1447.

1055 51. Haigler, C.H., and Brown, R.M. (1986). Transport of rosettes from the golgi apparatus to the
1056 plasma membrane in isolated mesophyll cells ofZinnia elegans during differentiation to tracheary
1057 elements in suspension culture. Protoplasma *134*, 111–120. https://doi.org/10.1007/bf01275709.

1058 52. Zhang, Y., Nikolovski, N., Sorieul, M., Vellosillo, T., McFarlane, H.E., Dupree, R., Kesten,
1059 C., Schneider, R., Driemeier, C., Lathe, R., et al. (2016). Golgi-localized STELLO proteins
1060 regulate the assembly and trafficking of cellulose synthase complexes in Arabidopsis. Nat.
1061 Commun. *7*, 11656. https://doi.org/10.1038/ncomms11656.

1062 53. Paredez, A.R., Somerville, C.R., and Ehrhardt, D.W. (2006). Visualization of Cellulose
1063 Synthase Demonstrates Functional Association with Microtubules. Science *312*, 1491–1495.
1064 https://doi.org/10.1126/science.1126551.

1065 54. Scheible, W.-R., Eshed, R., Richmond, T., Delmer, D., and Somerville, C. (2001).
1066 Modifications of cellulose synthase confer resistance to isoxaben and thiazolidinone herbicides
1067 in Arabidopsis Ixr1 mutants. Proceedings of the National Academy of Sciences *98*, 10079–
1068 10084. https://doi.org/10.1073/pnas.191361598.

1069 55. Zhou, Q., Lai, Y., Bacaj, T., Zhao, M., Lyubimov, A.Y., Uervirojnangkoorn, M., Zeldin,
1070 O.B., Brewster, A.S., Sauter, N.K., Cohen, A.E., et al. (2015). Architecture of the
1071 synaptotagmin–SNARE machinery for neuronal exocytosis. Nature *525*, 62–67.
1072 https://doi.org/10.1038/nature14975.

1073 56. Brunger, A.T. (2005). Structure and function of SNARE and SNARE-interacting proteins. Q
1074 Rev Biophys *38*, 1–47. https://doi.org/10.1017/s0033583505004051.

1075 57. Rothman, J.E., Krishnakumar, S.S., Grushin, K., and Pincet, F. (2017). Hypothesis –
1076 buttressed rings assemble, clamp, and release SNAREpins for synaptic transmission. FEBS Lett.
1077 *591*, 3459–3480. https://doi.org/10.1002/1873-3468.12874.

1078 58. Cho, W.J., Jeremic, A., and Jena, B.P. (2005). Size of Supramolecular SNARE Complex:
1079 Membrane-Directed Self-Assembly. J. Am. Chem. Soc. *127*, 10156–10157.
1080 https://doi.org/10.1021/ja052442m.

1081 59. Cho, W.J., Lee, J., Zhang, L., Ren, G., Shin, L., Manke, C.W., Potoff, J., Kotaria, N.,
1082 Zhvania, M.G., and Jena, B.P. (2011). Membrane-directed molecular assembly of the neuronal
1083 SNARE complex. J. Cell. Mol. Med. *15*, 31–37. https://doi.org/10.1111/j.1582-
1084 4934.2010.01152.x.

1085 60. Giddings, T.H., and Staehelin, L.A. (1988). Spatial relationship between microtubules and
1086 plasma-membrane rosettes during the deposition of primary wall microfibrils in Closterium sp.
1087 Planta *173*, 22–30. https://doi.org/10.1007/bf00394482.

1088 61. Lindeboom, J.J., Nakamura, M., Saltini, M., Hibbel, A., Walia, A., Ketelaar, T., Emons,
1089 A.M.C., Sedbrook, J.C., Kirik, V., Mulder, B.M., et al. (2019). CLASP stabilization of plus ends
1090 created by severing promotes microtubule creation and reorientation. J. Cell Biol. *218*, 190–205.
1091 https://doi.org/10.1083/jcb.201805047.

1092 62. Crowell, E.F., Bischoff, V., Desprez, T., Rolland, A., Stierhof, Y.-D., Schumacher, K.,
1093 Gonneau, M., Höfte, H., and Vernhettes, S. (2009). Pausing of Golgi Bodies on Microtubules
1094 Regulates Secretion of Cellulose Synthase Complexes in Arabidopsis. Plant Cell *21*, 1141–1154.
1095 https://doi.org/10.1105/tpc.108.065334.

1096 63. Martinière, A., Gayral, P., Hawes, C., and Runions, J. (2011). Building bridges: formin1 of
1097 Arabidopsis forms a connection between the cell wall and the actin cytoskeleton. Plant J. *66*,
1098 354–365. https://doi.org/10.1111/j.1365-313x.2011.04497.x.

1099 64. Geelen, D., Leyman, B., Batoko, H., Sansebastiano, G.-P.D., Moore, I., and Blatt, M.R.
1100 (2002). The abscisic acid-related SNARE homolog NtSyr1 contributes to secretion and growth:
1101 evidence from competition with its cytosolic domain. Plant Cell *14*, 387–406.
1102 https://doi.org/10.1105/tpc.010328.

1103 65. Grefen, C., Chen, Z., Honsbein, A., Donald, N., Hills, A., and Blatt, M.R. (2010). A novel
1104 motif essential for SNARE interaction with the K(+) channel KC1 and channel gating in
1105 Arabidopsis. Plant Cell *22*, 3076–3092. https://doi.org/10.1105/tpc.110.077768.

1106 66. Hoffmann, N., King, S., Samuels, A.L., and McFarlane, H.E. (2021). Subcellular
1107 coordination of plant cell wall synthesis. Dev. Cell *56*, 933–948.
1108 https://doi.org/10.1016/j.devcel.2021.03.004.

1109 67. Cosgrove, D.J. (2015). Plant expansins: diversity and interactions with plant cell walls. Curr.
1110 Opin. Plant Biol. *25*, 162–172. https://doi.org/10.1016/j.pbi.2015.05.014.

1111 68. Baskin, T.I. (2005). ANISOTROPIC EXPANSION OF THE PLANT CELL WALL. Annu.
1112 Rev. Cell Dev. Biol. *21*, 203–222. https://doi.org/10.1146/annurev.cellbio.20.082503.103053.

1113 69. Lindeboom, J.J., Nakamura, M., Hibbel, A., Shundyak, K., Gutierrez, R., Ketelaar, T.,
1114 Emons, A.M.C., Mulder, B.M., Kirik, V., and Ehrhardt, D.W. (2013). A Mechanism for
1115 Reorientation of Cortical Microtubule Arrays Driven by Microtubule Severing. Science *342*,
1116 1245533. https://doi.org/10.1126/science.1245533.

1117 70. Baas, P.W., Rao, A.N., Matamoros, A.J., and Leo, L. (2016). Stability properties of neuronal
1118 microtubules. Cytoskeleton *73*, 442–460. https://doi.org/10.1002/cm.21286.

1119 71. Tojima, T., Itofusa, R., and Kamiguchi, H. (2014). Steering Neuronal Growth Cones by
1120 Shifting the Imbalance between Exocytosis and Endocytosis. The Journal of Neuroscience *34*,
1121 7165–7178. https://doi.org/10.1523/jneurosci.5261-13.2014.

1122 72. Brown, A.-L., Wilkins, O.G., Keuss, M.J., Hill, S.E., Zanovello, M., Lee, W.C., Bampton,
1123 A., Lee, F.C.Y., Masino, L., Qi, Y.A., et al. (2022). TDP-43 loss and ALS-risk SNPs drive mis-
1124 splicing and depletion of UNC13A. Nature *603*, 131–137. https://doi.org/10.1038/s41586-022-
1125 04436-3.

1126 73. Ma, X.R., Prudencio, M., Koike, Y., Vatsavayai, S.C., Kim, G., Harbinski, F., Briner, A.,
1127 Rodriguez, C.M., Guo, C., Akiyama, T., et al. (2022). TDP-43 represses cryptic exon inclusion
1128 in the FTD–ALS gene UNC13A. Nature *603*, 124–130. https://doi.org/10.1038/s41586-022-
1129 04424-7.

1130 74. Liu, X., and Henty-Ridilla, J.L. (2022). Multiple roles for the cytoskeleton in ALS. Exp.
1131 Neurol. *355*, 114143. https://doi.org/10.1016/j.expneurol.2022.114143.

1132 75. Zhang, S., Cooper-Knock, J., Weimer, A.K., Shi, M., Moll, T., Marshall, J.N.G., Harvey, C.,
1133 Nezhad, H.G., Franklin, J., Souza, C. dos S., et al. (2022). Genome-wide identification of the
1134 genetic basis of amyotrophic lateral sclerosis. Neuron *110*, 992-1008.e11.
1135 https://doi.org/10.1016/j.neuron.2021.12.019.

1136 76. Curtis, M.D., and Grossniklaus, U. (2003). A Gateway Cloning Vector Set for High-
1137 Throughput Functional Analysis of Genes in Planta. Plant Physiol. *133*, 462–469.
1138 https://doi.org/10.1104/pp.103.027979.

1139 77. Shaner, N.C., Campbell, R.E., Steinbach, P.A., Giepmans, B.N.G., Palmer, A.E., and Tsien,
1140 R.Y. (2004). Improved monomeric red, orange and yellow fluorescent proteins derived from
1141 Discosoma sp. red fluorescent protein. Nat. Biotechnol. *22*, 1567–1572.
1142 https://doi.org/10.1038/nbt1037.

1143 78. Kirik, V., Herrmann, U., Parupalli, C., Sedbrook, J.C., Ehrhardt, D.W., and Hülskamp, M.
1144 (2007). CLASP localizes in two discrete patterns on cortical microtubules and is required for cell
1145 morphogenesis and cell division in Arabidopsis. J. Cell Sci. *120*, 4416–4425.
1146 https://doi.org/10.1242/jcs.024950.

1147 79. Assaad, F.F., Huet, Y., Mayer, U., and Jürgens, G. (2001). The Cytokinesis Gene KEULE
1148 Encodes a Sec1 Protein That Binds the Syntaxin Knolle. J. Cell Biol. *152*, 531–544.
1149 https://doi.org/10.1083/jcb.152.3.531.

1150 80. Clough, S.J., and Bent, A.F. (1998). Floral dip: a simplified method for Agrobacterium -
1151 mediated transformation of Arabidopsis thaliana. Plant J. *16*, 735–743.
1152 https://doi.org/10.1046/j.1365-313x.1998.00343.x.

1153 81. Logemann, E., Birkenbihl, R.P., Ülker, B., and Somssich, I.E. (2006). An improved method
1154 for preparing Agrobacterium cells that simplifies the Arabidopsis transformation protocol. Plant
1155 Methods *2*, 16. https://doi.org/10.1186/1746-4811-2-16.

1156 82. Ruhnow, F., Zwicker, D., and Diez, S. (2011). Tracking Single Particles and Elongated
1157 Filaments with Nanometer Precision. Biophys. J. *100*, 2820–2828.
1158 https://doi.org/10.1016/j.bpj.2011.04.023.

1159

1160 **Acknowledgments:** We thank Michael Davidson for the kind gift of the tdTomato construct. We
1161 thank Zdeněk Lánský, Johnathan Cooper-Knock and Masayoshi Nakamura for advice
1162 and insightful comments.

1163 **Funding:**

1164 National Institutes of Health grant R15GM137247-01 (VK)

1165 National Institutes of Health grant R01GM123259-01 (DWE)

1166

1167 **Author contributions:**

1168 Conceptualization: JJL, RG, VK, DWE

1169 Methodology: JJL, RG, VK, DWE

1170 Investigation: JJL, RG, VK, DWE

Visualization: JJL, RG, DWE

Funding acquisition: VK, DWE

Writing – original draft: JJL, RG, DWE

Writing – review & editing: JJL, RG, VK, DWE

Competing interests: The authors declare no competing interests.

Data and materials availability: Biological material, raw data, processed data and MATLAB scripts used for the analysis are available upon request.

1179 **Figures**

1180 **Figure 1**

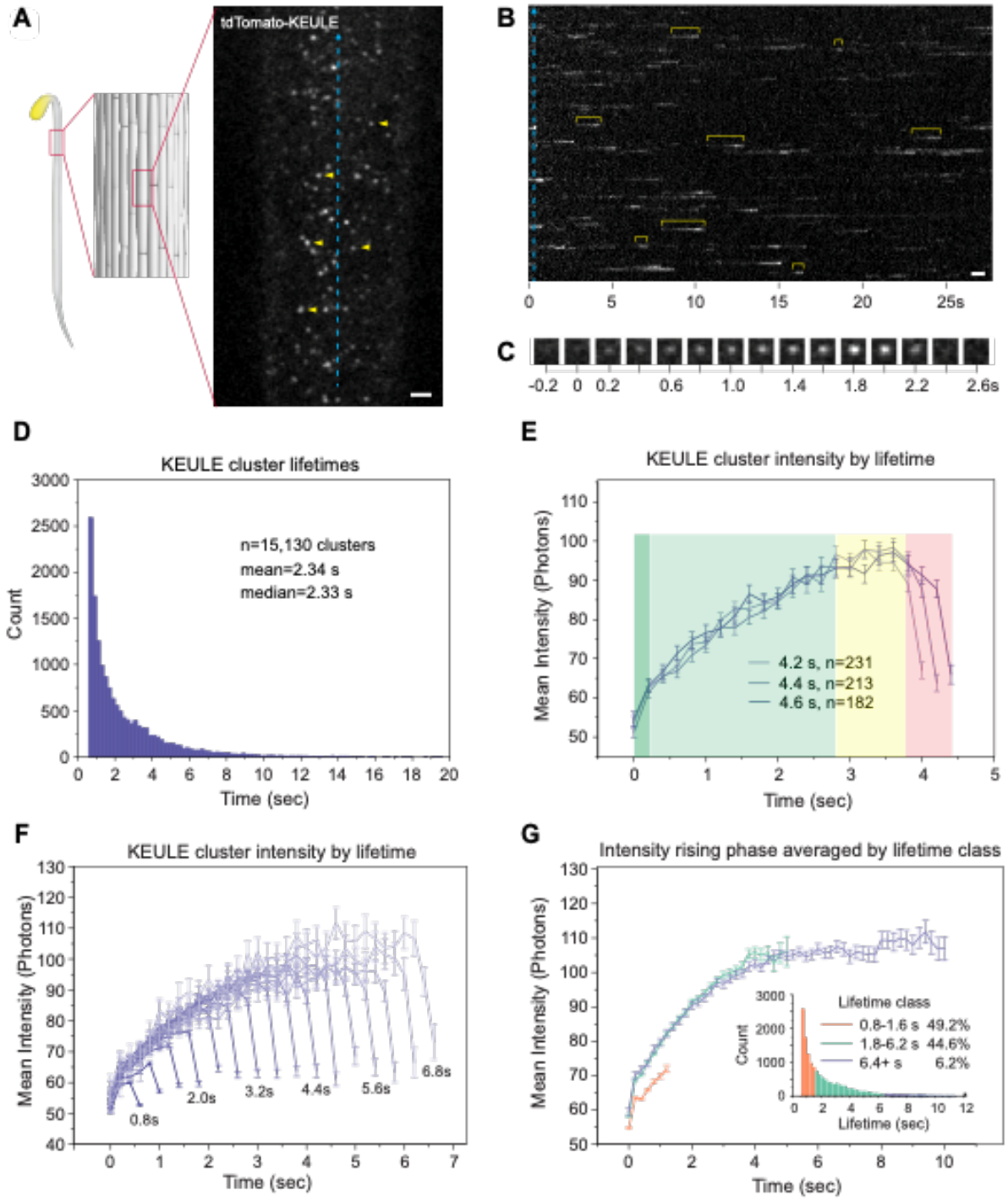

1181

1182 **Fig. 1. KEULE assembly dynamics at the plasma membrane**. (**A**) Distribution of tdTomato-KEULE
1183 signal at the plasma membrane of etiolated hypocotyl cells in *Arabidopsis*. Arrowheads point out
1184 individual clusters of labeled KEULE protein. (**B**) Kymograph of the tdTomato-KEULE signal intensity
1185 over time as sampled over the transect line shown in (**A**) (blue dashes). The yellow brackets highlight
1186 several individual tdTomato-KEULE clusters. (**C**) Example of tdTomato-KEULE cluster intensity over
1187 time. (**D**) Histogram of KEULE cluster lifetimes in 200 ms bins. n = 15,130 clusters. (**E**) Average
1188 tdTomato-KEULE cluster signal intensity with a lifetime of 4.2, 4.4 and 4.6 s. Note the initial rapid
1189 increase in signal over the first acquisition step (darker green), the more gradual, near linear, ramp up
1190 (green) to a plateau (yellow), followed by abrupt loss to non-detection (red). n = 231, 213,182 clusters for
1191 4.2, 4.4 4.8 s, respectively. (**F**) Average tdTomato-KEULE cluster signal intensity with lifetimes ranging
1192 from 0.8 to 6.8 s. n = 15,397 clusters in total, ranging from 4992 clusters for 0.8 s to 122 for 6.8 s. (**G**)
1193 Average signal intensities of tdTomato-KEULE clusters in three cumulative lifetime ranges, 0.8 to 1.6 s,
1194 1.8 to 6.2 s and 6.4+ s. The inset shows the lifetime distribution histogram of tdTomato-KEULE cluster
1195 lifetimes with the lifetime ranges color coded. n = 15,130 clusters. All data in panels D-G acquired from
1196 12 cells from 12 seedlings. Error bars are S.E. Scale bars are 2 µm.

1197

1198 **Figure 2**

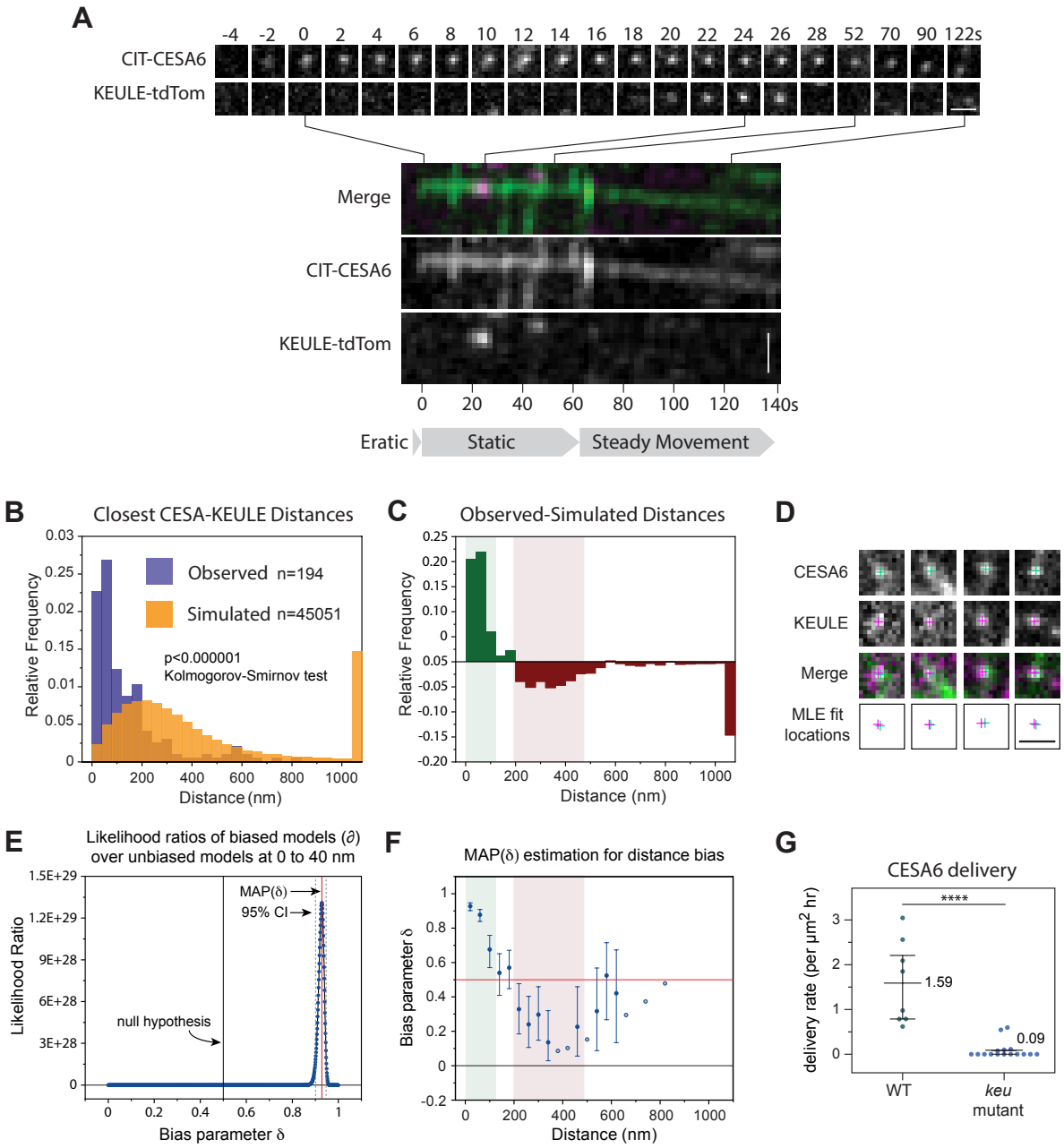

1199
1200

Fig. 2. KEULE is spatially associated with and required for CSC delivery to the plasma membrane. (**A**) CESA exocytosis event. (Top panel) Time series (top panel) and kymograph (bottom panel) of tdTomato-KEULE and CIT-CESA6 during a CESA exocytosis event. The kymograph shows evidence for CSC-vesicle tethering at the plasma membrane (start of static phase) and successful CSC delivery to the plasma membrane as an active complex (steady movement phase, see text). (**B**) Distribution of distances between the positions of CIT-CESA6 signals at start of static phase and the nearest tdTomato-KEULE cluster, as estimated by MLE PSF fitting. Data shown both for observed CIT-CESA6 locations and simulated random locations. (**C**) Differences of the observed vs expected CESA6-KEULE distance frequencies in (**B**), portraying over- and under-representation (green and red respectively). (**D**) Examples of colocalization and fitted positions for events in (**B**). (**E**) Bayesian likelihood ratios of the observed frequency of distances between 0 and 40 nm given bias δ over $\delta(0.5)$. The position of the peak value indicates the most likely, or maximum a posteriori probability (MAP), value for the bias δ for the observed frequency given the expected frequency. (**F**) Bayesian analysis of the MAP(δ) for each distance bin, MAP(δ) = 0.5 indicates no difference from expected. Error bars are 95% confidence intervals expressed as the highest posterior density (HPD, the shortest interval containing 95% of the probability density). (**G**) CESA6 delivery rates in wild type and *keule* mutant cells. Whiskers are quartiles. **** $p<0.0001$ Wilcoxon 2-sample test. In panels B-F, n = 194 CESA exocytosis events in 8 cells from 8 seedlings for observed data. For simulated data, n = 45051 randomized CESA exocytosis locations in the same KEULE channel data sets. In panel G, n = 8 cells from 8 seedlings for WT and 16 cells from 16 plants for *keule*. Scale bars are 1 μm.

1221 **Figure 3**

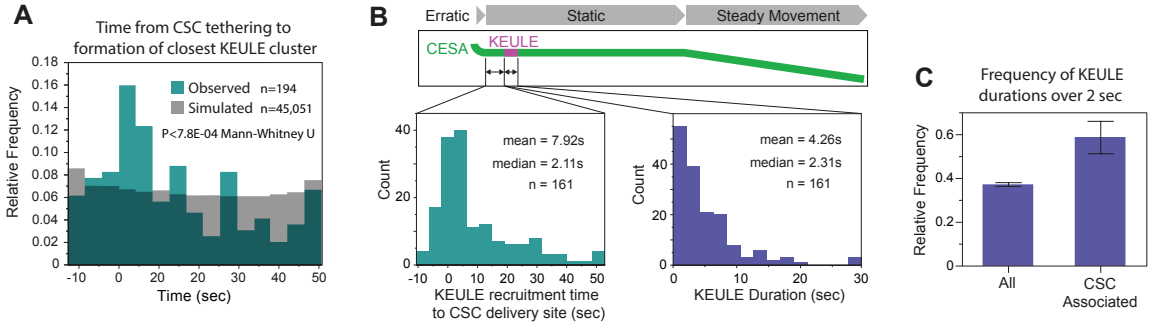

1222

1223 **Fig. 3. KEULE cluster appearance is temporally associated with CSC appearance at the plasma**
1224 **membrane.** (**A**) Comparison of the waiting time distribution from CSC signal stabilization until the
1225 detection of the nearest tdTomato-KEULE cluster in observed and simulated data. n = 194 CSC delivery
1226 events in 8 cells from 8 plants. (**B**) KEULE dynamics in the context of CSC delivery to the plasma
1227 membrane. Histograms of waiting times (left pane) and lifetimes of tdTomato-KEULE clusters co-
1228 localized with CSC delivery events (right pane). n = 161 CSC delivery events in 8 cells from 8 plants for
1229 observed data, n = 45,051 simulated CSC delivery events applied to the same data sets. (**C**) KEULE
1230 cluster durations for all events and those associated with CSC delivery, compared by relative frequency of
1231 durations over 2 seconds. n = 13766 for all KEULE clusters, n = 180 for KEULE clusters associated with
1232 CSC delivery. Whiskers are exact binomial 95% confidence intervals, p = 6.1E-09 Fishers' exact test.

1233 **Figure 4**

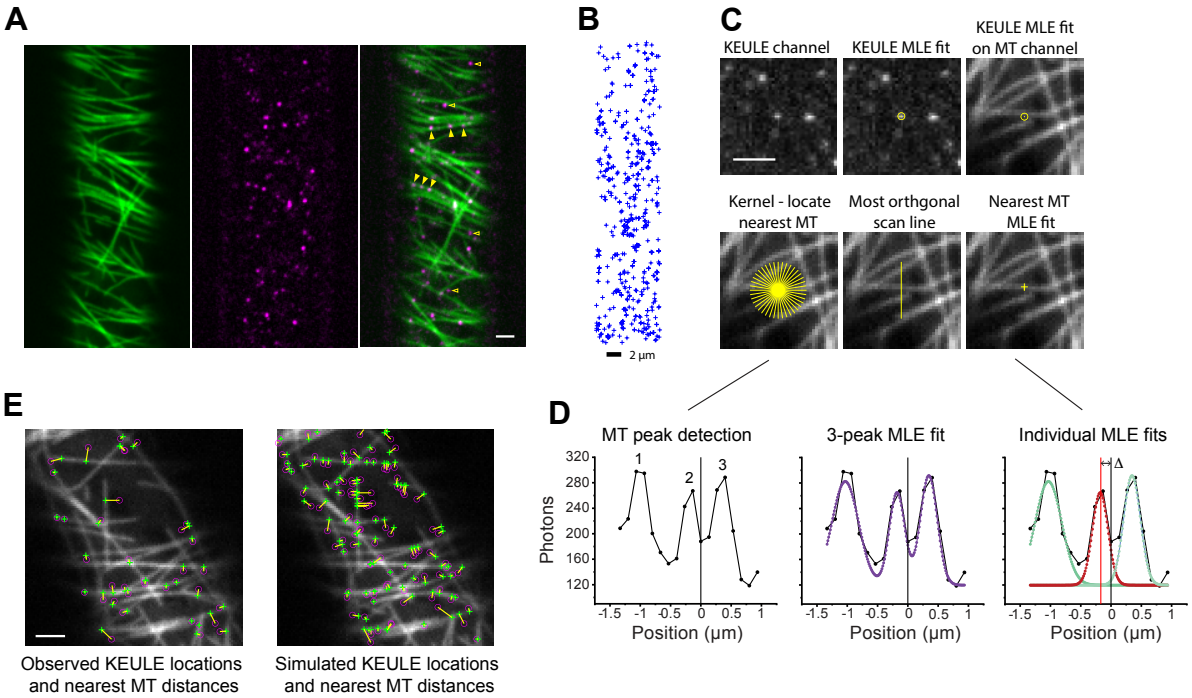

1234
1235 **Fig. 4. Microtubule dependent distribution of exocytosis events.** (**A**) Images of GFP-TUA5 and
1236 tdTomato-KEULE signal in epidermal cells. Arrowheads indicate examples of apparent co-localization of
1237 signal. (**B**) Spatial patterning of tdTomato-KEULE clusters over the range of 36.8 seconds. Crosses show
1238 positions of MLEwG fits. (**C**) Steps in the routine employed to calculation the distance from a KEULE
1239 cluster to the center of the nearest microtubule distance. (**D**) Steps in quasi-1-dimensional MLEwG fitting
1240 of microtubule signal along the most-orthogonal scan line of a rotating filter. (**E**) Overlay of a
1241 microtubule channel image and pairs of markers for MLE fit locations of KEULE clusters and the center
1242 of the nearest microtubule in observed data (left) and for simulated random KEULE locations (right).
1243 KEULE cluster detects from -5 to + 5 frames from the microtubule image are shown. Scale bars are 2 µm.

1244 **Figure 5**

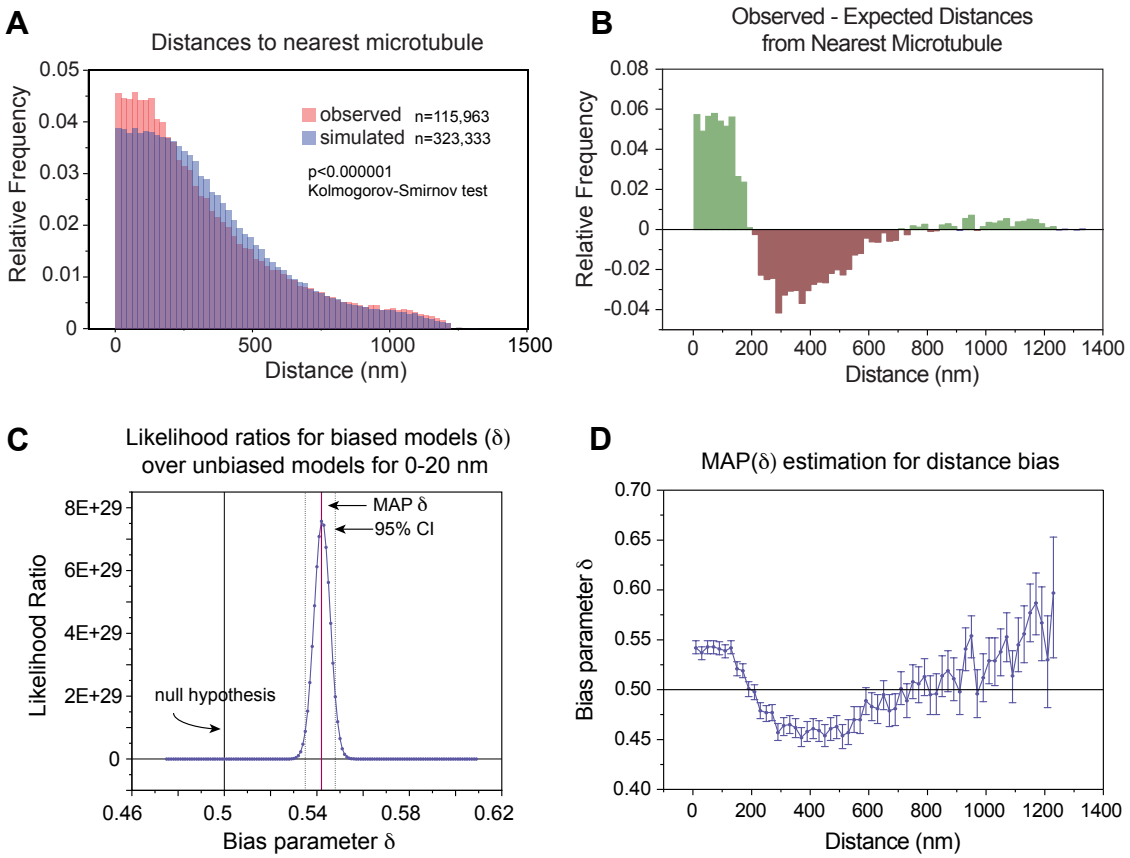

1245

1246 **Fig. 5. Bayesian analysis of microtubule bias for exocytosis events.** (**A**) Comparison of the
1247 distributions of KEULE-nearest microtubule distances for observed and simulated data. n = 115,963
1248 KEULE clusters in 14 cells from 14 plants. (**B**) Differences of the observed vs expected KEULE-
1249 microtubule distance frequencies shown in (**A**), portraying the pattern of over- and under-representation
1250 (green and red respectively). (**C**) Bayesian likelihood ratios of the observed frequency of KEULE-
1251 microtubule distances between 0 and 20 nm given bias δ over δ(0.5). (**D**) Bayesian analysis of the
1252 MAP(δ) of each distance bin. Data acquired from 14 cells in 14 seedlings. n = 115,963 KEULE clusters
1253 in 14 cells from 14 plants. Error bars are 95% confidence intervals expressed as HPD.

1254 **Figure 6**

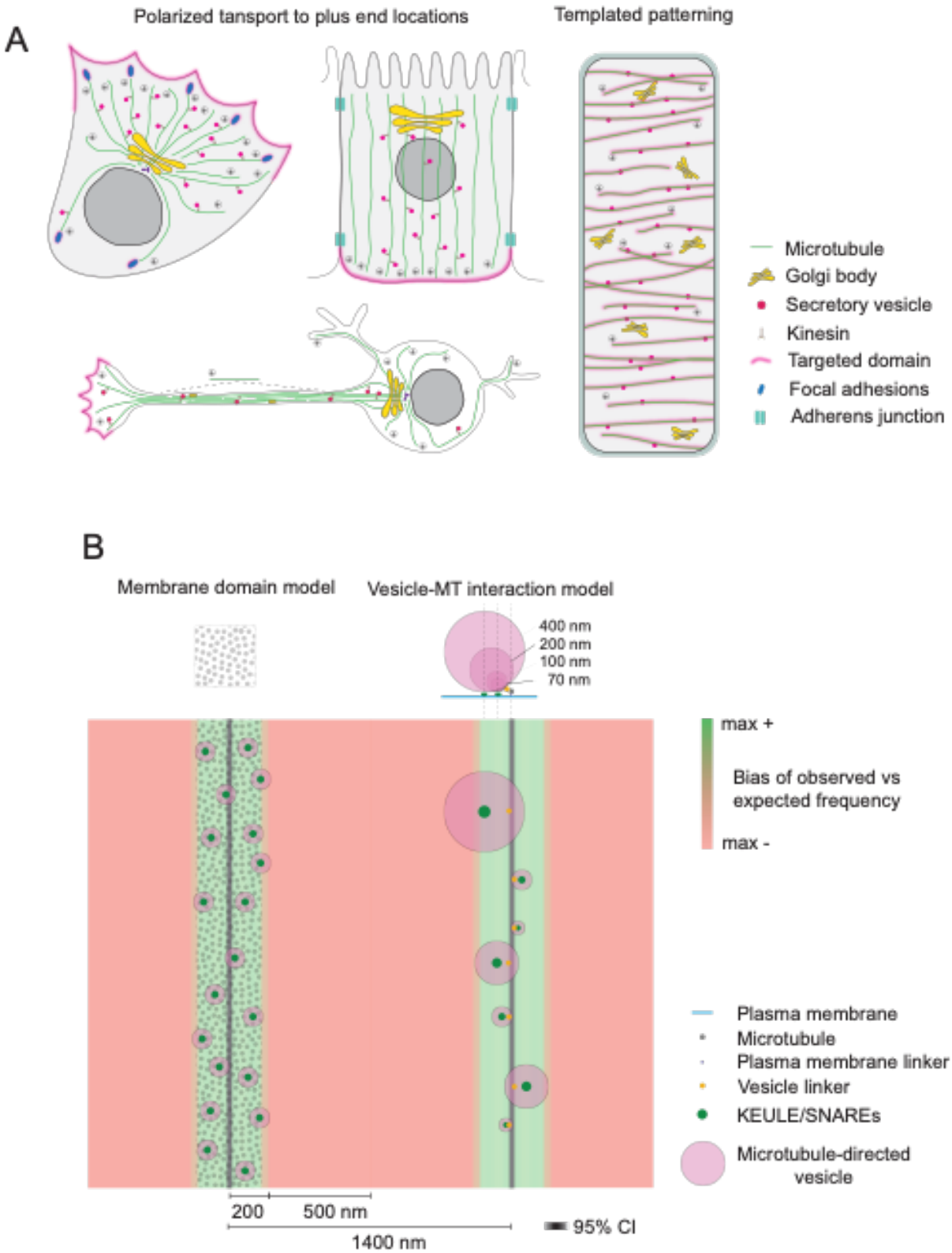

1255

1256 **Fig. 6. Patterning of exocytosis by microtubule arrays. (A)** Schematic diagrams of
1257 microtubule-directed patterning of exocytosis. The three cells on the left show targeting of
1258 exocytosis by motor-driven transport of vesicles along polarized microtubule tracks to locations
1259 defined by their plus ends[3] . Clockwise from upper left: migrating fibroblast, epithelial cell,
1260 neuronal cell. By contrast, the diagram at far right shows an epidermal cell in the plant axis,
1261 where a 2-D array of microtubules at the cell cortex acts as a template that directs exocytosis in a
1262 complex but ordered pattern. The organization of the microtubule lattices defines this pattern.
1263 **(B)** Alternative models for spatial patterning of exocytosis by cortical microtubule arrays in plant
1264 cells. All structures are abstracted but depicted at approximate scale. Microtubules (grey) are
1265 shown spaced at the mean spacing that has been measured in the cortical arrays of growing cells
1266 in the hypocotyl epidermis of dark grown *Arabidopsis* seedings[61]. The likelihood of exocytosis
1267 marked by dynamic KEULE clusters is shown as a red-green heat map as scaled from the
1268 observed over-representation and under-representation of KEULE clusters compared to that
1269 expected from the null hypothesis of a random distribution (depicted in Fig. 5B). The two sides
1270 of the diagram depict alternative models to explain the measured spatial dimensions of the
1271 domains enriched in exocytosis. On the right, the measured extent of the enriched domain is
1272 determined by the interaction exocytotic vesicle with microtubules, where those vesicles have a
1273 wide range of sizes. On the left, microtubules establish a membrane domain that extends
1274 approximately 180 nm on either side where proteins needed for vesicle capture or exocytosis are
1275 concentrated. These models are not mutually exclusive. The grey-scale bar at lower right depicts
1276 the mean 95% confidence interval for the measured distances of KEULE clusters to microtubule
1277 centers.
1278

1279 **Supplemental Materials**

1280 **Figure S1**

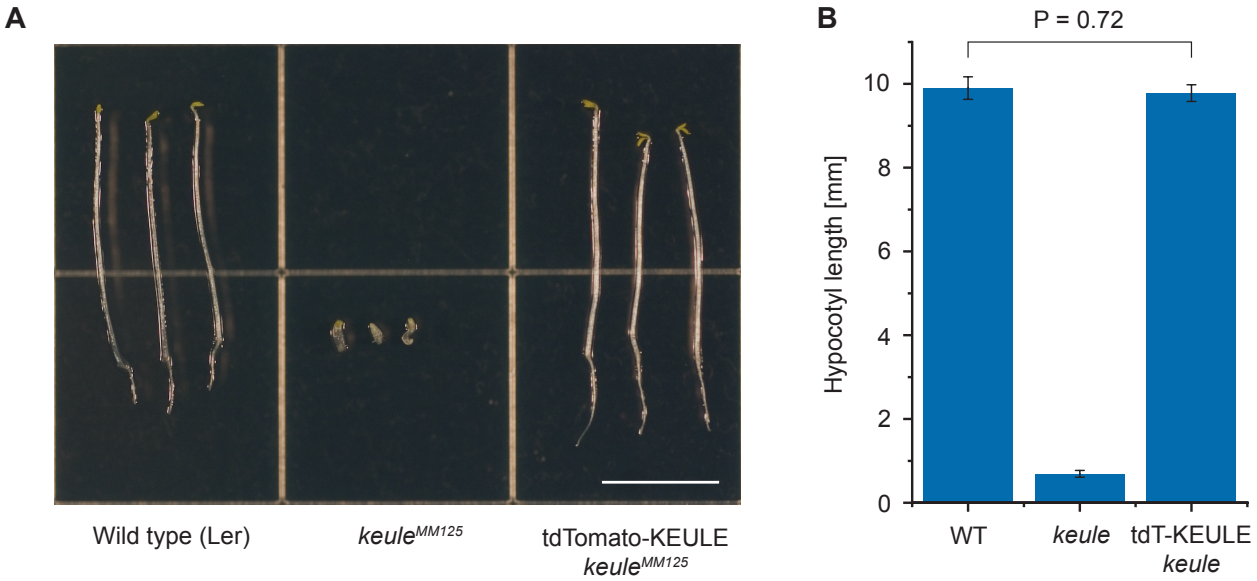

1281

1282 **Fig. S1. Complementation of the *keule* mutation. (A)** Seedlings of indicated genotypes were grown in
1283 the dark for 5 d. The recessive *keule*^{mm125} allele is seedling lethal; mutant seedlings have bloated,
1284 multinucleate cells. Expression of a tdTomato-tagged version of KEULE, expressed under the control of
1285 the native upstream regulatory element, complemented the *keule* mutation in dark-grown seedlings. Scale
1286 bar, 5 mm. **(B)** Hypocotyl elongation in 5-day-old dark-grown seedlings. Rescued seedlings were
1287 comparable to wild-type (n = 50 plants per genotype, P = 0.72 by t-test). Error bars represent SEM.

1288 **Figure S2**

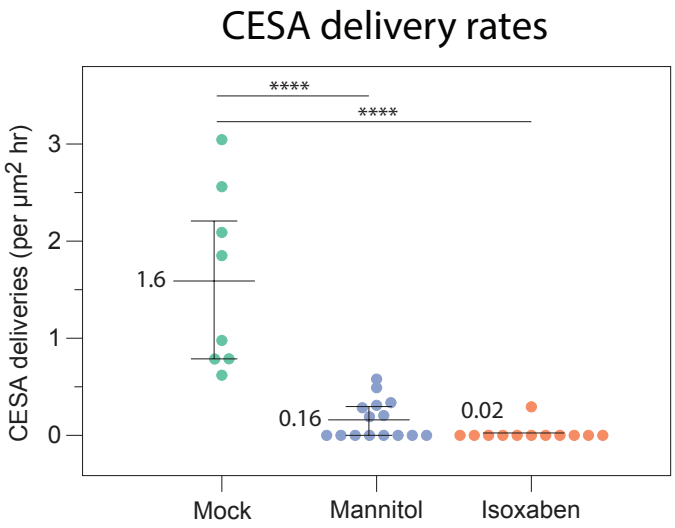

1289

1290 **Fig. S2. CSC delivery rates.** CSC delivery rates to the plasma membrane of cells expressing tdTomato-
1291 KEULE and CIT-CESA6 after treatment with 0.01% DMSO (mock), 200 mM mannitol or 100 nM
1292 isoxaben. See Methods for treatment durations. Values are means, whiskers are quartiles. Mock: n = 8
1293 cells from 8 seedlings, 208 delivery events observed in 1570 μm^2 total area over 0.0828 hr. Mannitol: n =
1294 15 cells from 15 seedlings, 11 delivery events observed in 880 μm^2 total area over 0.0793 hr. Isoxaben: n
1295 = 12 cells from 12 seedlings, 2 delivery events observed in 996 μm^2 total area over 0.0793 hr. ****
1296 $p<0.0001$, Wilcoxon two sample test.

1297 **Figure S3**

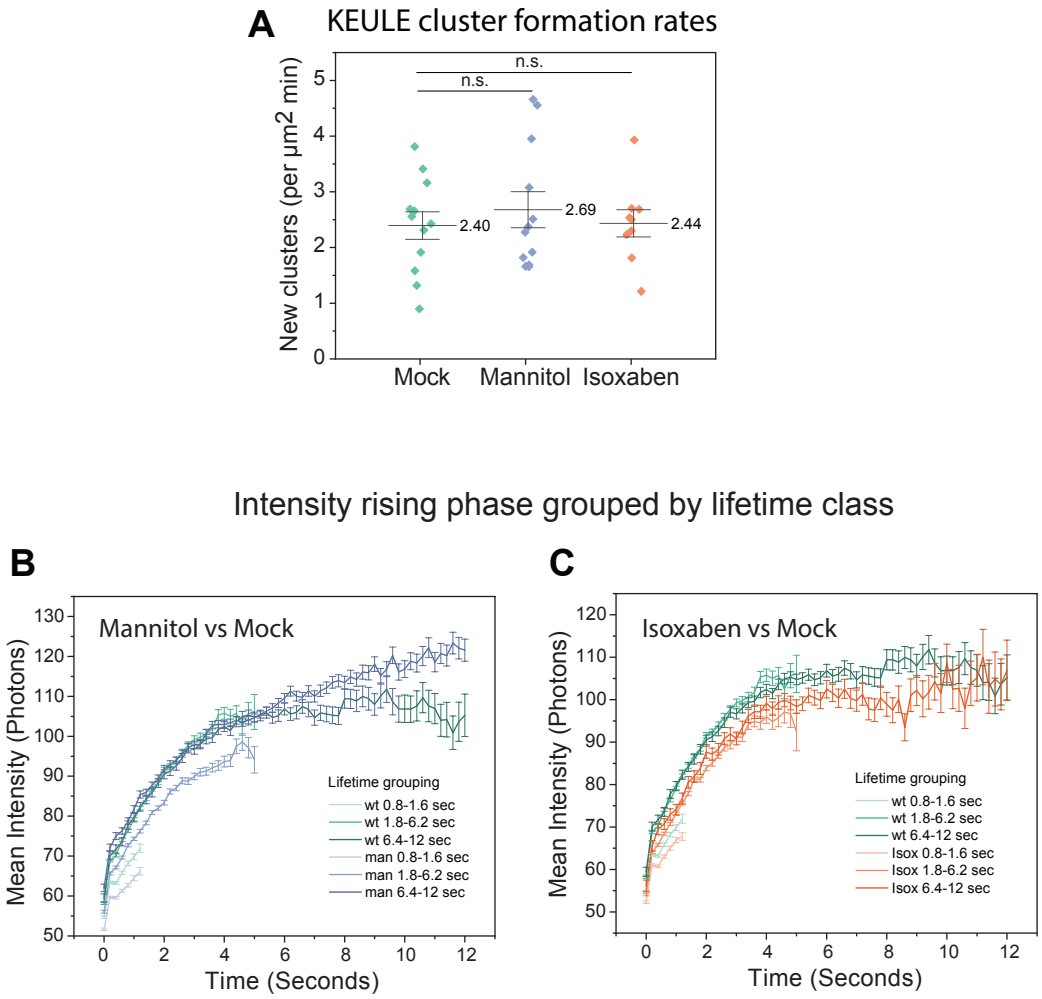

1298
1299

1300 **Fig. S3. Intensity of dynamics of tdTomato-KEULE clusters by lifetime.** (**A**) Average tdTomato-
1301 KEULE cluster signal intensity with lifetimes ranging from 0.8 to 6.8 s for mock, mannitol treatment. and
1302 isoxaben treatment. Whiskers are means and quartiles. n.s. p>0.05 Wilcoxon two sample test. (**B** and **C**)
1303 Comparison of average signal intensities of tdTomato-KEULE clusters in three cumulative lifetime
1304 ranges, 0.8 to 1.6 s, 1.8 to 6.2 s and 6.4 to 12.2 s, between (**B**) mock vs mannitol treatment, and (**C**) mock
1305 vs isoxaben treatment. Mock: n = 15,130 clusters observed in 12 cells from 12 plants. Mannitol: n =
1306 35,496 clusters observed in 15 cells from 15 plants. Isoxaben: n = 25,251 clusters observed in 12 cells
1307 from 12 plants. Error bars are SEM.

1308

Figure S4

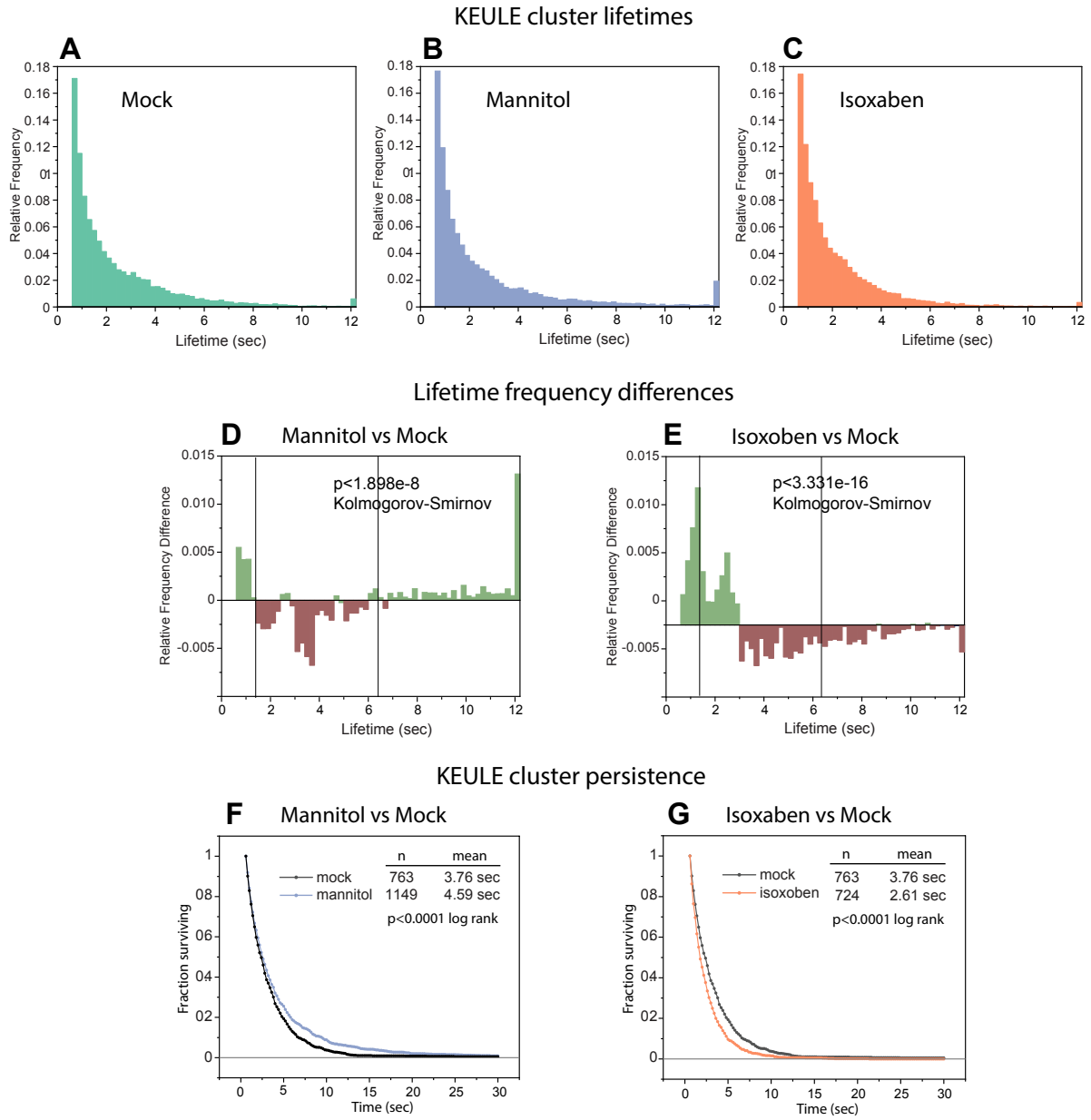

Fig. S4. KEULE cluster lifetimes. (**A** to **C**) Lifetime distribution of tdTomato-KEULE clusters in mock (**A**), mannitol (**B**) and isoxaben (**C**) treated cells. (**D** and **E**) Difference in relative lifetime frequency between mannitol and mock (**D**), and isoxaben and mock (**E**). Vertical lines indicate the lifetime classes in Figure 1G. (**F**) Formation rates of new tdTomato-KEULE clusters. Values are means. (**G** and **H**) Comparison of the fraction of remaining tdTomato-KEULE clusters that were present in the first frame of the movie for mannitol to mock (**G**) and isoxaben to mock. Mock: n = 763 clusters observed in 12 cells from 12 plants. Mannitol: n = 1149 clusters observed in 15 cells from 15 plants. Isoxaben: n = 724 clusters observed in 12 cells from 12 plants.

Figure S5

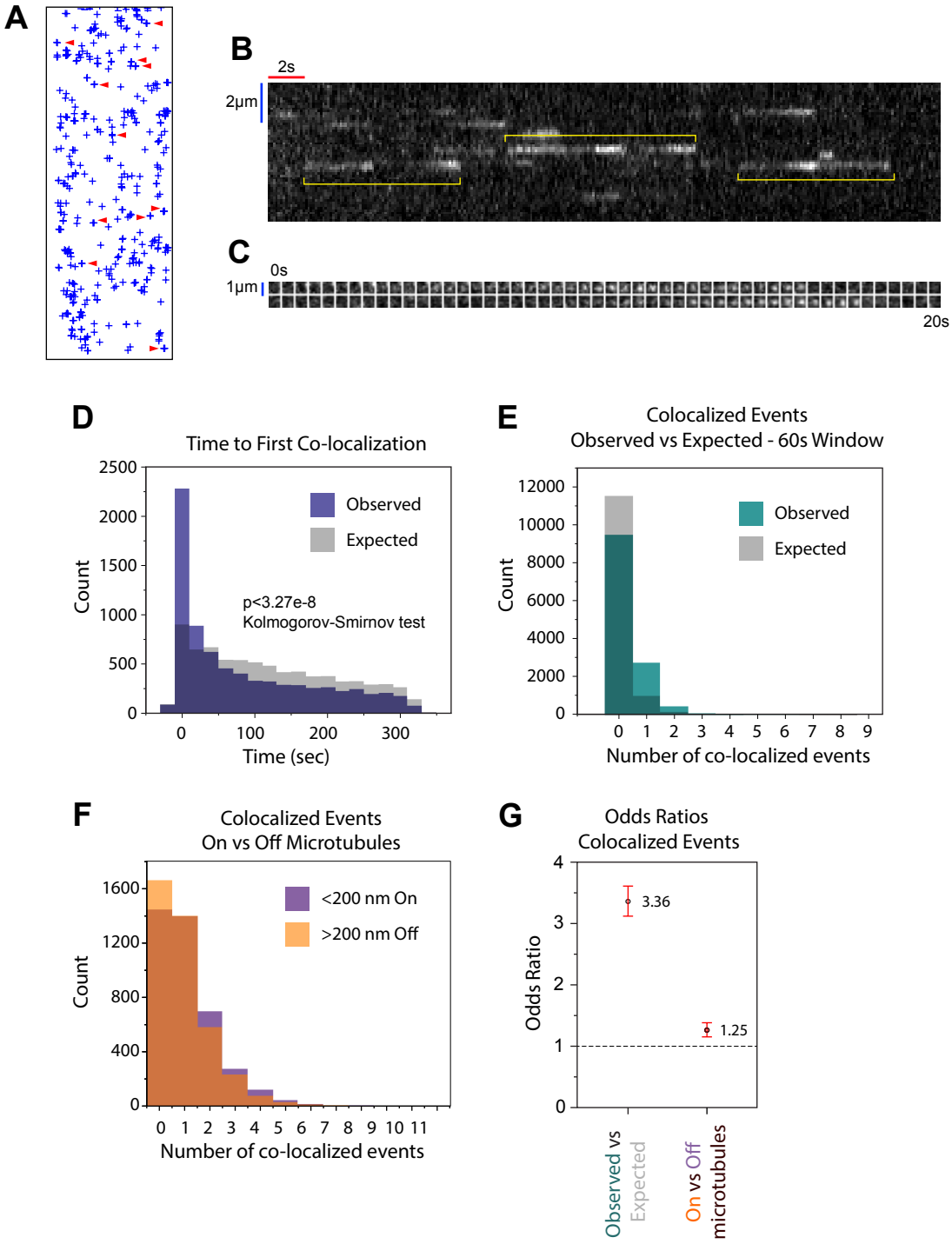
A
B
2s
2μm
C
0s
1μm
20s
D
Time to First Co-localization
Observed
Expected
p<3.27e-8
Kolmogorov-Smirnov test
Count
Time (sec)
E
Colocalized Events
Observed vs Expected - 60s Window
Observed
Expected
Count
Number of co-localized events
F
Colocalized Events
On vs Off Microtubules
<200 nm On
>200 nm Off
Count
Number of co-localized events
G
Odds Ratios
Colocalized Events
Odds Ratio
3.36
1.25
Observed vs Expected
On vs Off microtubules

Fig. S5 KEULE cluster hot spots. (**A**) Map of tdTomato-KEULE cluster detections over x minutes. Crosses are positions determined by MLEwG fitting. Arrowheads indicate examples of repeat detects at the same location, or hot spots. (**B**) Kymograph of tdTomato-KEULE signal along a 3 pixel wide transect line. Yellow brackets indicate examples of repeated KEULE cluster formation at the same location. (**C**) Individual image frames at a hot spot, 200 msec intervals over 20 seconds. (**D**) Distributions of waiting times for a second cluster to appear at the same location as a previous cluster, as defined by a stringent co-localization cutoff distance of 133 nanometers. The distributions for observed data and randomly simulated data are shown in purple and grey, respectively. Note that the observed intervals are significantly skewed to shorter intervals as compared to those in the simulated data ($p<3.27E-8$ Kolmogorov-Smirnov test). n = 12,719 clusters in 17 cells from 17 plants. (**E**) Distributions of the number of co-localized events observed at each KUELE cluster location within 60 seconds of the formation of the first cluster. Colocalization events were 3.36 more frequent in observed data (green) than expected by chance alone (grey), as determined by odds ratio analysis (see panel (**G**)). n = 9458 clusters in 17 cells from 17 plants. (F) Distributions of KEULE colocalization events either on or off microtubules on observed data. The distance threshold for microtubule association was < 200 nm. Sequential KEULE cluster co-localization was 1.25 times more frequent for KEULE events associated with microtubules than for those not associated with microtubules, as determined by odds ratio analysis (see panel (G)). n = 4000 clusters on microtubules and 4866 clusters off microtubules in 17 cells from 17 plants. (G) Odds ratios and 95% confidence intervals for the data shown in panels (G) and (F). The dotted line indicates the odds ratio expected for the null hypothesis of no different from random.

1345 **Figure S6**

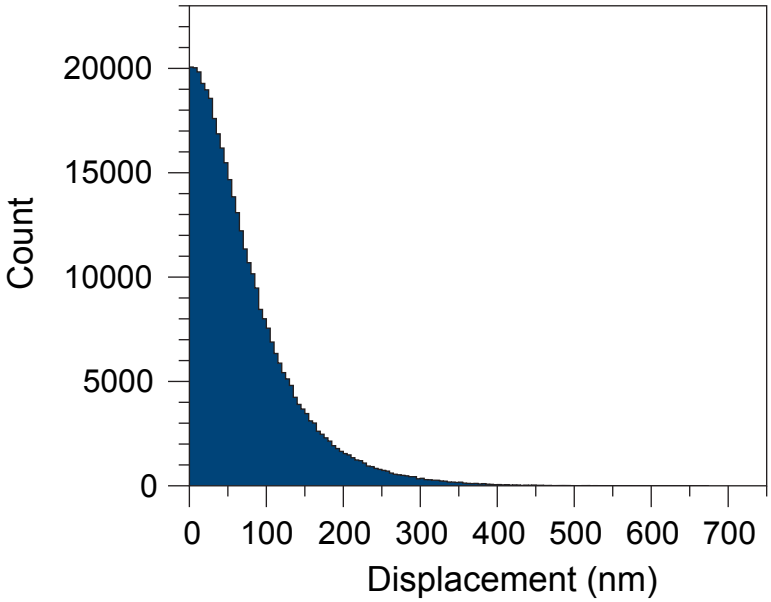

1346

1347 **Fig. S6.** Frame-to-frame displacements of tdTomato-KEULE clusters in 200 ms streaming acquisitions. n
1348 = 283,127 displacements for 15,130 clusters observed in 12 cells from 12 plants.

1349

1350 **Figure S6**

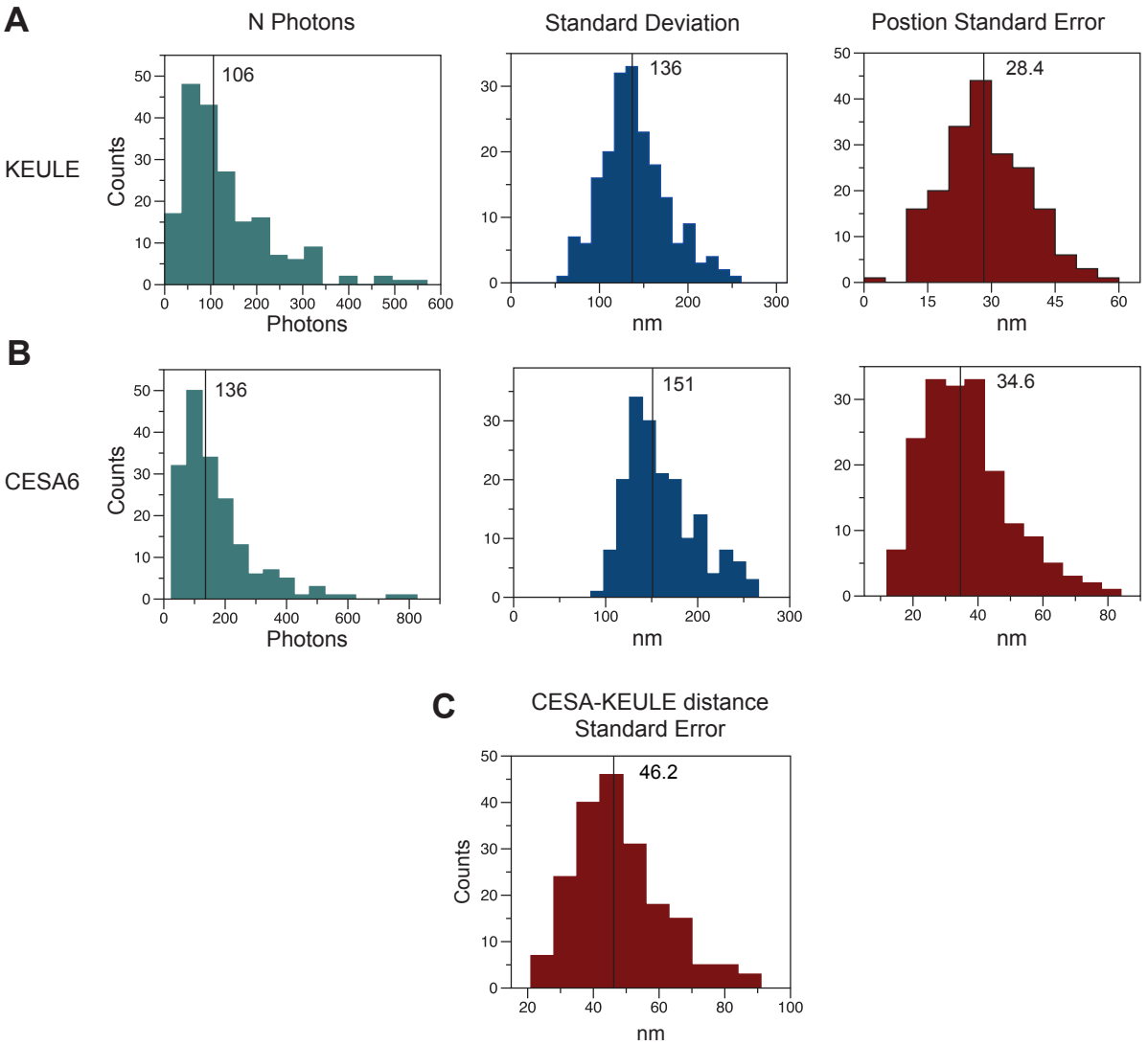

1351

1352 **Fig. S6. Fit parameters for CSC vesicles in the tethering frame and the nearest KEULE clusters to**
1353 **these tethering sites.** (**A**) Distributions of fit parameters for MLEwG fits of tdTomato-KEULE clusters.
1354 (**B**) Distributions of fit parameters for MLEwG fits of CIT-CESA6 signal. (**C**) Distribution of standard
1355 errors for KEULE to microtubule distance measurements. Black lines and values indicate means. n = 194

1356

1357 **Figure S7**

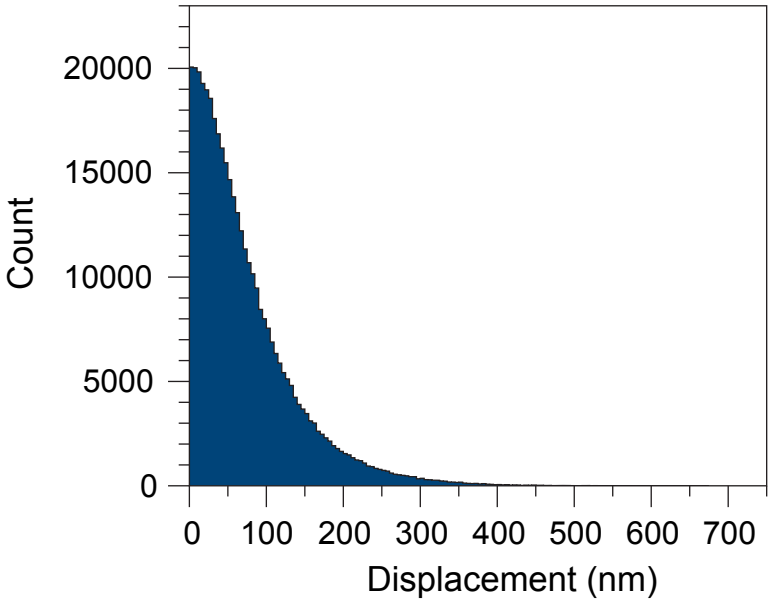

1358

1359 **Fig. S7.** Frame-to-frame displacements of tdTomato-KEULE clusters in 200 ms streaming acquisitions. n
1360 = 283,127 displacements for 15,130 clusters observed in 12 cells from 12 plants.

1361

1362

1363 **Figure S8**

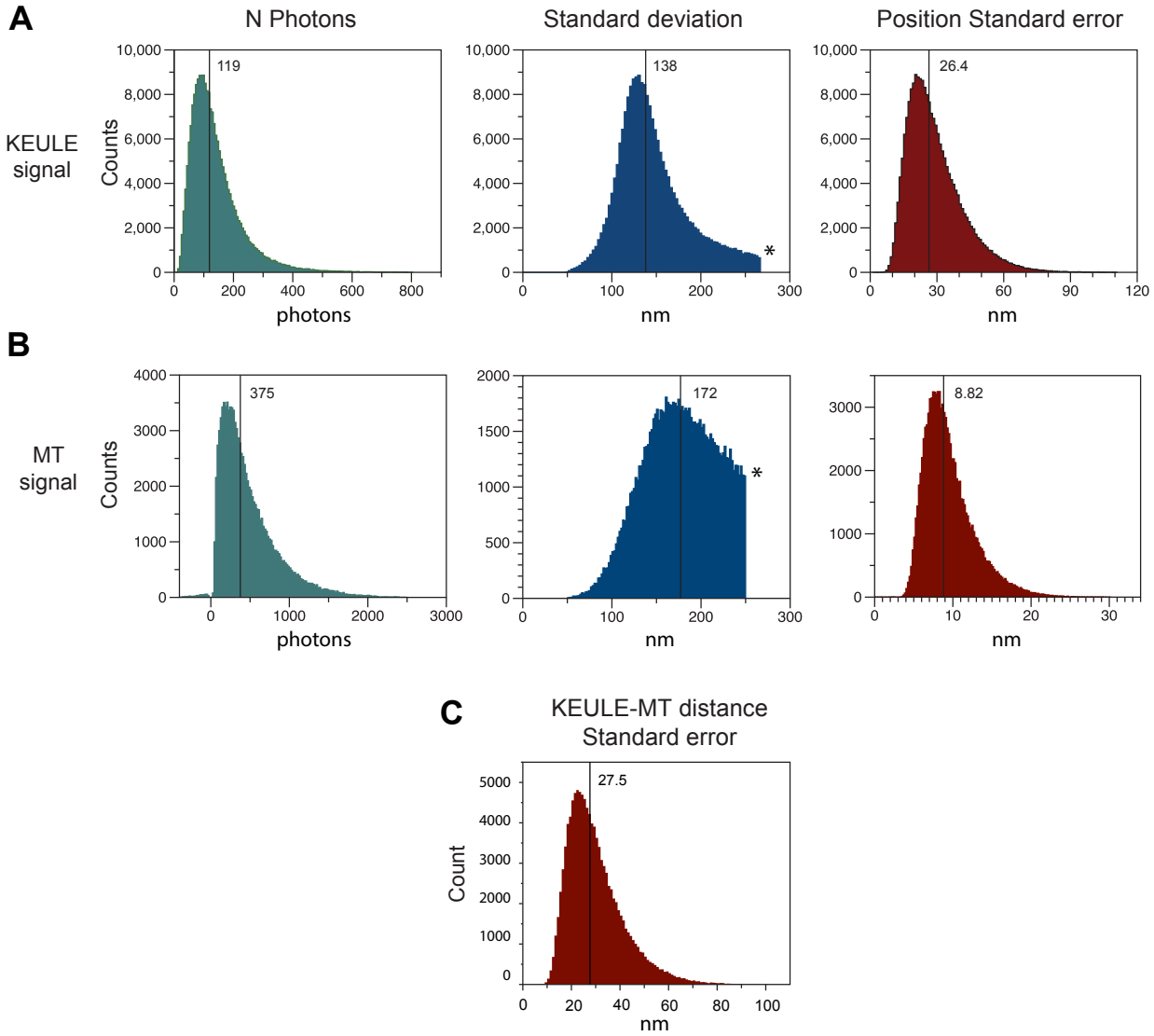

1364

1365 **Fig. S8. Fit parameters for KEULE to microtubule distances used for localization analysis.** (**A**) Fit
1366 parameters for MLEwG fits of tdTomato-KEULE clusters. (**B**) Fit parameters for MLEw1dG fitting of
1367 microtubule signal. (**C**) Standard error of KEULE to microtubule distance measurements. Black lines and
1368 values indicate means. *Truncations of standard deviation distributions are due to cutoff values used to
1369 filter and exclude bad fits due to signal patterns that complicate localization analysis. Bad fits for
1370 tdTomato-KEULE signal occur where more than one tdTomato-KEULE cluster are close in proximity,
1371 and bad fits for microtubule signal occur where microtubules are dense and where they intersect in
1372 complex patterns. n = 115,963 KEULE clusters, nearest microtubule locations and KEULE-microtubule
1373 distances observed in 14 cells from 14 plants.

1374 **Movie S1.**

1375 **tdTomato-KEULE cluster dynamics.** Spinning disk confocal images of tdTomato cluster formation and
1376 loss at the plasma membrane of an epidermal hypocotyl cell in a dark grown *Arabidopsis* seedling. To
1377 reduce noise, images were averaged with a running 3-frame window. Streaming acquisition at 5
1378 frames/sec. Playback at 4x real time.

1379 **Movie S2.**

1380 **MLE Gaussian fits of tdTomato-KEULE clusters.** Spinning disk confocal images of tdTomato-
1381 KEULE clusters in an epidermal hypocotyl cell of a dark grown *Arabidopsis* seedling. Magenta circles
1382 indicate an automated detection of a KEULE cluster. For each of these detects the coordinates of the
1383 signal centroid number of detected photons were estimated by MLE Gaussian fitting (see methods).
1384 Streaming acquisition at 5 frames/sec. Playback at 10x real time.
1385

1386 **Movie S3.**

1387 **KEULE localization to CSC delivery events.** Spinning disk confocal images of co-expressed tdTomato-
1388 KEULE and Cit-CESA6. Filled arrowheads point to locations of tracked CSC signal. Empty arrowheads
1389 point to co-localized KEULE clusters that appear shortly after appearance and positional stabilization of
1390 CESA6 signal. 2 second acquisition intervals. 3-frame running average. Playback at 10x real time.
1391

1392 **Movie S4.**

1393 **MLE Gaussian fits of tdTomato-KEULE clusters and EGFP-TUA5 labeled microtubules.** Spinning
1394 disk confocal images of co-expressed tdTomato-KEULE and EGFP-TUA5 labeled microtubules. White
1395 circles indicate automated KEULE signal detects. The position of each cluster at the first frame of
1396 stabilization was estimated at a sub-pixel level if MLE Gaussian fitting. 1 second acquisition intervals.
1397 Playback at 20x real time.